

ESD-TR-66-207
ESTI FILE COPY

ESD-TR-66-207

ESD RECORD COPY

RETURN TO
SCIENTIFIC & TECHNICAL INFORMATION DIVISION
(ESTI), BUILDING 1211

ESD ACCESSION LIST

ESTI Call No. AL 52555
Copy No. 1 of 2 cys.

2

Solid State Research

1966

Prepared under Electronic Systems Division Contract AF 19(628)-5167 by

Lincoln Laboratory

MASSACHUSETTS INSTITUTE OF TECHNOLOGY

Lexington, Massachusetts



AD0639064

The work reported in this document was performed at Lincoln Laboratory, a center for research operated by Massachusetts Institute of Technology, with the support of the U.S. Air Force under Contract AF 19(628)-5167.

This report may be reproduced to satisfy needs of U.S. Government agencies.

Distribution of this document is unlimited.

Non-Lincoln Recipients

PLEASE DO NOT RETURN

Permission is given to destroy this document
when it is no longer needed.

2

Solid State Research

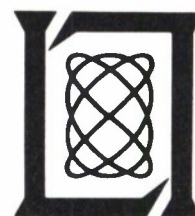
1966

Issued 18 August 1966

Lincoln Laboratory

MASSACHUSETTS INSTITUTE OF TECHNOLOGY

Lexington, Massachusetts



ABSTRACT

This report covers in detail the solid state research work at Lincoln Laboratory for the period 1 February through 30 April 1966. The topics covered are Solid State Device Research, Optical Techniques and Devices, Materials Research, and Physics of Solids.

Accepted for the Air Force
Franklin C. Hudson
Chief, Lincoln Laboratory Office

INTRODUCTION

1. SOLID STATE DEVICE RESEARCH

Electron beam excitation of mixed crystals of $\text{CdS}_x\text{Se}_{1-x}$ has produced laser oscillations at several wavelengths in the visible part of the spectrum from 0.69 to 0.49 μ , with up to 20 W of peak output power and as high as 11-percent power efficiency at 4.2°K. The samples were made from high-purity, single-crystal, vapor-grown platelets of seven different compositions varying from pure CdSe to pure CdS. Laser emission always occurred at a wavelength within 10 \AA of the peak of the 30- to 50- \AA wide dominant spontaneous 1_1 line. In all cases, both the spontaneous and stimulated radiation were strongly polarized with $E \perp c$. In CdSe, for 50-keV electrons, a minimum threshold beam current of 50 mA/cm², a maximum peak output power of 16 W, and a power efficiency of 8 percent were obtained. These values are typical also for the various mixed crystals studied. For pure CdS, however, the minimum threshold beam current was 1000 mA/cm² and the efficiency was only 0.7 percent. This anomalously high threshold and low efficiency were observed in all CdS samples from several different crystals, and as yet remain unexplained.

We observed spontaneous emission at wavelengths from 3 to 15 μ , and laser emission at 3.8 and 4.1 μ from $\text{Cd}_x\text{Hg}_{1-x}\text{Te}$ crystals at 12°K excited optically by the radiation from a GaAs diode laser. The sample surface irradiated by the GaAs laser beam was a (110) plane, and two parallel cleaved faces perpendicular to this plane formed the Fabry-Perot cavity. Current pulses of a few microseconds duration were applied to the GaAs diode. The onset of coherent emission occurred at a GaAs diode current of about 1 A, which corresponds to approximately 0.3 W of 0.84- μ radiation. An equivalent threshold current of about 50 mA is estimated if it is assumed that one electron-hole pair is produced by each photon which is absorbed by the sample.

We report also the successful pumping of InSb and CdSe lasers at liquid helium temperature using a pulsed xenon flashlamp. Peak flashlamp power densities in the wavelength interval of 0.6 to 0.2 μ of 15 kW cm⁻² are obtainable with an f/1.5 one-to-one imaging system. For InSb, we observed minimum threshold power densities of about 700 W cm⁻² with a 500- μ cavity. Well-defined thresholds of about 4 kW cm⁻² for a 500- μ cavity were observed in CdSe.

Power output, efficiency, and spatial distribution of coherent emission from PbS and PbSe diode lasers have been measured at about 7°K. A peak power of 24 mW at 2 A with 2- μ sec current pulses was measured for PbS. This corresponds to an external quantum efficiency of about 4 percent. The CW power output at 0.6 A was 2 mW. For PbSe, a peak power of 3 mW at 2 A (2- μ sec pulses), corresponding to an external quantum efficiency of 1 percent, and a CW power output of 0.2 mW at 0.8 A were measured.

Introduction

Epitaxial layers of high-purity GaAs have been prepared using an open-tube vapor transport system in a two-zone furnace with Ga placed in the high-temperature zone and the GaAs seeds inserted into the lower temperature deposition region. Pure H₂ from a palladium-alloy diffuser is bubbled through AsCl₃ and the resultant gas mixture is passed through the reaction tube. Hall mobilities as high as 70,000 cm²/V-sec have been obtained in samples with free carrier concentrations of $7.3 \times 10^{14} \text{ cm}^{-3}$ at 77°K.

A model for GaAs transferred-electron microwave amplifiers has been developed using a three-slope piecewise-linear approximation for the drift velocity vs electric field curve. Good quantitative agreement is obtained with the DC I-V characteristics and with the admittance and gain data over the frequency range 2.5 to 5GHz for devices in the 50-μ length range.

II. OPTICAL TECHNIQUES AND DEVICES

Photon statistics of a laser near threshold have been measured, taking into account spontaneous emission noise and residual modulation. The experimental data are in excellent agreement with theoretical predictions of Glauber.

In the 10-μ spectral region, Cu-doped Ge has been used as a background-limited detector. By the proper choice of high-purity starting material and dopant concentration, the noise equivalent power of typical detectors has been reduced to $2.5 \times 10^{-14} \text{ W}$ for a 3- by 3-mm device, cooled to liquid helium temperature. The marked improvement in sensitivity is a result of the increased carrier lifetime obtained in the crystal preparation.

Argon laser discharge anomalies have been studied further using electron densities obtained from Stark linewidths of neutral transitions. The anomalous variation of the discharge and light emission with pressure and magnetic field has now been explained using a theoretical model which takes into account a transition of ion motion from free-fall to ambipolar diffusion at increased electron gas pressures.

A carbon dioxide laser has been operated as a sealed-off system yielding a power output of 10 W at an efficiency of 7 percent. The output beam is a single TEM₀₀ mode operating on a single emission line. Tube lifetime is on the order of 4 to 8 hours, degrading to 50-percent power output for extended periods of operation.

III. MATERIALS RESEARCH

A method has been developed for growing large single crystals of iodine by sublimation in a closed ampule. The ampule, which is tapered to a narrow tip at the upper end, is immersed in a water bath heated to ~75°C. As the water level slowly falls because of evaporation, a single crystal is nucleated at the narrow tip, which is the first part of the ampule to emerge from the water.

The partial pressures of $\text{Te}_2(\text{g})$ in equilibrium with Ge-Te samples containing between 1 and 52 atomic-percent Te have been determined by measuring the optical density of the vapor as a function of the temperature of the condensed phases. Results show that, in contrast to SnTe, at sufficiently high temperatures the homogeneity range for GeTe(c) includes compositions of less than 50 atomic-percent Te.

A new phase transformation in InSb has been identified by superconductivity measurements on samples first annealed at high pressures and temperatures and then quenched to low temperature before releasing the pressure. For pressures of 37 and 52 kbar, the phase transformation occurs at $308 \pm 7^\circ\text{C}$ and $287 \pm 12^\circ\text{C}$, respectively. Below the transformation temperature, the high-pressure phase is tetragonal InSb(II), with superconducting transition temperature of about 2.1°K . For the high-temperature phase, whose structure has not yet been determined, the superconducting transition temperature is 4.0° to 4.1°K .

The phase diagram of the pseudo-binary InSb-InTe system at 37 kbar has been investigated by x-ray and superconductivity measurements on samples annealed at 500°C and quenched to room temperature before releasing the pressure. At 37 kbar, there are single-phase regions with rocksalt structure which extend from 60 to at least 80 mole-percent InTe, and from pure InTe to at least 90 mole-percent InTe. The data so far available do not establish whether these two regions are separated by a miscibility gap, or whether there is complete solid solubility between 60 and 100 mole-percent InTe.

The x-ray structure factor for MgO and the atomic form factors of magnesium and oxygen in MgO have been determined by computer analysis of x-ray diffraction data for MgO powders at ten temperatures between room temperature and 500°C . The results for oxygen are generally in good agreement with the theoretical form factor given by Tokonami, although there is some discrepancy between theory and experiment at low diffraction angles.

The threshold energy for laser oscillation in a ruby rod fabricated from a vapor-grown crystal containing 0.01% Cr_2O_3 was found to be 25 J at approximately 90°K . Under the same conditions, the laser threshold for a Czochralski-grown rod containing 0.05% Cr_2O_3 was 28 J. The fact that the thresholds are approximately the same, in spite of the difference in Cr^{+3} concentration, indicates that the crystal quality of the vapor-grown material is quite high.

New or improved analytical techniques have been developed for determining the major constituents in several ternary systems. These include a more accurate method for analyzing rare earth cobalt oxides by complexometric titrations, x-ray fluorescence methods for lanthanum cobalt oxide and iron-nickel-copper thin films, and microprobe analysis of $\text{CdSe}_x\text{S}_{1-x}$ alloys.

IV. PHYSICS OF SOLIDS

The reflectivity measurements in ReO_3 have now been extended beyond 12 eV, out to 22 eV. In this new range, the reflectivity peaks up to 15 percent at about 14 eV, then slowly drops down to about 9 percent at 22 eV.

Introduction

The experimental investigation of the band structure of GaSe is continuing. Using spectrographic techniques for higher resolution, the excitonic magnetoabsorption spectrum is now being studied.

The large polaron effects in the interband magnetoabsorption of InSb, which were predicted theoretically, have now been observed. These results constitute the first direct and unambiguous observation of polaron self-energy effects. Corroborative evidence for the polaron has also been obtained from the observed anomalies in the intraband magnetoabsorption near the longitudinal optical phonon frequency.

The application of a magnetic field to the piezo-optical technique results in a marked improvement in the sensitivity of magneto-optical measurements. The power of this technique has been demonstrated in preliminary results in Ge and InSb at room temperature.

A detailed analysis of the oscillatory optical reflectivity associated with interband transitions between Landau levels has been carried out. This theory accounts for the differences between the lineshapes observed in bismuth and graphite.

The microwave cyclotron resonance measurements in PbSe have now been extended to n-type material. The conduction band parameters have been determined by matching the experimental results to classical skin effect theory.

The effect of both mass anisotropy and nonlocal field corrections on microwave helicon propagation in n-PbTe has been investigated experimentally and theoretically. As a result of the ellipsoidal band structure, large nonlocal field corrections (including a form of Landau damping) are found even for propagation along the magnetic field.

The propagation of 9-GHz longitudinal ultrasonic waves has been studied in n-InSb at temperatures between 4.2° and 36°K and in magnetic fields up to 25 kG for several crystal orientations and electron concentrations, with particular emphasis on the electronic contribution to the attenuation and velocity of the ultrasonic wave. These experiments have yielded a direct determination of the piezoelectric constant e_{14} and the conduction band deformation potential for InSb, the values being 0.06 C/m^2 and -4.5 eV , respectively.

It is known from experiment that the magnetic field dependence of the frequency of luminescence from a semiconductor depends on the concentration of free carriers. A variational treatment has been carried out which invokes Thomas-Fermi screening to explain this free carrier effect.

The Fourier expansion technique has now been used to study the energy bands of crystals with diamond crystalline symmetry. A specific application of the method to silicon yields a band model which is consistent with all experimental data.

The calculation for the classical ground spin state of a magnetic spinel with nonmagnetic ions on the A-sites is continuing. Stable spin configurations in a section of the next-nearest-neighbor exchange-parameter space have been determined. The resulting prediction for the spinel ordering in ZnCr_2Se_4 does not agree with experiment, and the calculation is being extended in order to obtain the observed configuration.

The magnetic resonance linewidth, measured in the paramagnetic region, of the insulating spinels CdCr_2S_4 and CdCr_2Se_4 has been compared with a theoretical expression based only on dipolar spin-spin interactions, and relatively good agreement is found. The slightly higher theoretical values may result from the neglect of the next-nearest-neighbor interactions.

Extraordinary simplifications occur over the quantum calculation when calculating the high-temperature expansions of the susceptibility χ and specific heat C with the classical Heisenberg model. This classical model is useful in these cases, since χ and C are extremely insensitive to the spin value.

The work on symmetry of transport coefficients is continuing. A simple method is indicated for obtaining the space-time symmetry restrictions on the field-dependent transport coefficients. Results are given for the thermo-galvanomagnetic coefficients.

Using a principle due to Frenkel for studying collective excitations of complex systems, results such as the "S-wave coupling" on the spin excitation spectrum of superconductors have been rederived. This technique is now being used to study electrical conduction in narrow bands.

The work on nonlinear optics is continuing. Stimulated Raman emission associated with the vibrational mode at 911 cm^{-1} has been observed in several calcium tungstate single crystals – both pure and Nd^{3+} -doped, at room temperature. Near 20°K , the pure calcium tungstate crystal emits stimulated Raman emission at 911 cm^{-1} , but the Nd-doped crystal emits at 83 cm^{-1} .

Measurements of second harmonic incoherent scattering have now been extended to the region above room temperature. The rapid decrease of the scattering to a plateau, with increasing temperatures, probably arises from the dissociation of molecular clusters.

The reported anomalously intense, polarized, and narrow-band microwave emission of interstellar OH is believed to be due to maser amplification of spontaneous emission. A model has been proposed for obtaining the necessary inverted population by means of near-ultraviolet pumping. A propagation analysis in the presence of a small galactic field indicates that a single, dominant, highly polarized elliptical or circular mode will grow in a given direction.

CONTENTS

Abstract	iii
Introduction	v
Organization	xiii
Reports by Authors Engaged in Solid State Research	xiv
I. SOLID STATE DEVICE RESEARCH	1
A. Efficient Visible Lasers of $\text{CdS}_x\text{Se}_{1-x}$ by Electron Beam Excitation	1
B. Spontaneous and Coherent Photoluminescence in $\text{Cd}_x\text{Hg}_{1-x}\text{Te}$	3
C. Incoherent Source Optical Pumping of Visible and Infrared Semiconductor Lasers	5
D. Pb Salt Diode Lasers	7
E. Preparation of High-Purity Epitaxial GaAs	7
II. OPTICAL TECHNIQUES AND DEVICES	11
A. Photoelectron Statistics Produced by Laser Above Threshold of Oscillation	11
B. Detectability of Cu-Doped Germanium	14
C. Argon Laser Discharge Anomalies	16
D. Single-Mode CO_2 Laser at 10.6μ	19
III. MATERIALS RESEARCH	21
A. Vapor Growth of Iodine Single Crystals	21
B. Partial Pressures of $\text{Te}_2(\text{g})$ in Equilibrium with $\text{Ge}_{1/2-\delta}\text{Te}_{1/2+\delta}(\text{c})$	23
C. New Phase Transformation in InSb at High Pressures and Temperatures	25
D. Pseudo-Binary InSb-InTe System at 37 kbar	26
E. Experimental Atomic Form Factors in MgO	27
F. Laser Properties of Vapor-Grown Ruby	30
G. Chemical Analysis	32
1. Complexometric Titrations	32
2. X-Ray Fluorescence Analysis	32
3. Electron Microprobe Analysis	33

IV. PHYSICS OF SOLIDS	35
A. Electronic Band Structure	35
1. Optical Constants of ReO_3	35
2. Exciton Structure and Zeeman Effects in GaSe at 1.5°K	35
3. Polaron Induced Anomalies in InSb	38
4. Observation of Polaron Resonance in Intraband Magnetoabsorption in InSb	38
5. Magneto-Piezo-Optical Studies in Semiconductors	39
6. Lineshape Analysis of the Magnetoreflexion Experiment	41
7. Magnetoplasma Cyclotron Resonance in PbSe	41
8. Luminescence in Magnetic Field of Excitons with Screened Coulomb Potential	41
9. Fourier Expansion for Energy Bands of Diamond Lattice	42
B. Magnetism	43
1. Classical Ground Spin States in Normal Cubic Spinel with Nonmagnetic A-Sites	43
2. Paramagnetic Resonance Linewidth in Chromium Spinel	46
3. High-Temperature Expansions for Spin Correlation Function in Classical Heisenberg Model	46
C. Transport Theory	48
1. Space-Time Symmetry of Transport Coefficients	48
2. Applications of Frenkel Variational Principle	52
D. Quantum Electronics	52
1. Stimulated Raman Emission in CaWO_4	52
2. Temperature Dependence of Incoherent Second Harmonic Light Scattering in Liquids	53
3. Maser Amplification of Interstellar OH Emission	54

ORGANIZATION

SOLID STATE DIVISION

A. L. McWhorter, *Head*
P. E. Tannenwald, *Associate Head*
M. J. Hudson, *Assistant*
E. P. Warekois
D. T. Stevenson*
T. C. Harman†

SOLID STATE THEORY

H. J. Zeiger, *Leader*
M. M. Litvak, *Assistant Leader*

Argyres, P. N.	Mason, V. J.
Dresselhaus, G. F.	Mason, W. C.
Houghton, B. H.*	Palm, B. I.*
Kaplan, T. A.	Stanley, H. E.*
Kleiner, W. H.	Trent, P. H.
Larsen, D. M.	Van Zandt, L. L.

OPTICS AND INFRARED

R. H. Kingston, *Leader*
R. J. Keyes, *Assistant Leader*

Bates, D. H.	Freed, C.
Bostick, H. A.	Longaker, P. R.
Carbone, R. J.	McGowan, J.
Dennis, J. H.	Zimmerman, M. D.

ELECTRONIC MATERIALS

J. B. Goodenough, *Leader*
J. M. Honig, *Associate Leader*
A. J. Strauss, *Assistant Leader*

Andrews, H. I.‡	Kafalas, J. A.
Arnott, R. J.	LaFleur, W. J.
Banus, M. D.	Lavine, M. C.*
Brebrick, R. F.	Longo, J. M.
Button, M. J.	Newman, W. A.
Cornwell, J. C.	O'Connor, J. R.
Defaney, E. J.	Owens, E. B.
Ehlers, H. H.	Paladino, A. E.
Fahey, R. E.	Plonko, M. C.
Farrell, L. B.	Pollard, E. R.‡
Ferretti, A.	Rabio, M. A.
Finn, M. C.	Raccah, P. M.
Fischler, S.	Reed, T. B.†
Germann, R. W.	Ridgley, D. H.
Hilsenrath, S.	Roddy, J. T.
Iseler, G. W.	Sohn, J. B.

SOLID STATE PHYSICS

J. G. Mavroides, *Leader*
G. B. Wright, *Assistant Leader*

Bermon, S.	Kolesar, D. F.
Burke, J. W.	Krag, W. E.
Carman, R. L.*	Mastromattei, E. L.
Dickey, D. H.	Menyuk, N.
Dresselhaus, M. S.	Parker, C. D.
Dwight, K., Jr.	Perry, F. H.
Feinleib, J.	Scouler, W. J.
Feldman, B.	Stickler, J. J.‡
Fulton, M. J.	Strahm, N. D.‡
Groves, S. H.	Thaxter, J. B.
Halpern, J.	Weber, R.
Johnson, E. J.	Weinberg, D. L.
Kernan, W. C.	

APPLIED PHYSICS

R. H. Rediker, *Leader*
J. O. Dimmock, *Associate Leader*
I. Melngailis, *Assistant Leader*

Butler, J. F.	Foyt, A. G.	Mooradian, A.	Walpote, J. N.‡
Calawa, A. R.	Grant, C. R.	Nill, K. W.‡	Ward, J. H. R., III
Carter, F. B.	Hinkley, E. D.	Palermo, J. S.	Wolfe, C. M.
Caswell, F. H.	Hurwitz, C. E.	Phelan, R. J.	Womac, J.‡
Clough, T. F.	Lindley, W. T.	Quist, T. M.	Youtz, P.
Donaldson, P. L.	McPhie, J. M.	Sullivan, F. M.	

* Part Time

† Leave of Absence

‡ Research Assistant

REPORTS BY AUTHORS ENGAGED IN SOLID STATE RESEARCH

15 February through 15 May 1966

PUBLISHED REPORTS

Journal Articles*

JA No.			
2570	Space-Time Symmetry of Transport Coefficients	W. H. Kleiner	Phys. Rev. <u>142</u> , 318 (1966), DDC 635328
2591	Properties of InAs Lasers	I. Melngailis R. H. Rediker	J. Appl. Phys. <u>37</u> , 899 (1966)
2605	Electrical Properties of Metal Oxides Characterized by "Hopping" Charge Carriers	J. M. Honig	J. Chem. Educ. <u>43</u> , 76 (1966)
2613A	Automatic Potentiometric EDTA and Redox Titrations for Determinations of Stoichiometry	M. C. Gardels J. C. Cornwell	Anal. Chem. <u>38</u> , 774 (1966)
2621	Superconductivity in the Transition Metal Carbides: $\text{Mo}_{4.8}\text{Si}_3\text{C}_{0.6}$, $\text{Mo}_{0.95}\text{Hf}_{0.05}\text{C}_{0.75}$ and Mo_2C	V. Sadagopan [†] H. C. Gatos	J. Phys. Chem. Solids <u>27</u> , 235 (1966)
2625	Cyclotron Resonance of Piezoelectric Polarons	D. M. Larsen	Phys. Rev. <u>142</u> , 428 (1966), DDC 635332
2640	Discussion of "Theory of Nonequilibrium Thermodynamics with Application to the Transport Processes in Solids," by M. R. El-Saden	J. M. Honig	Trans. ASME, J. Heat Transfer, Series C, <u>62</u> (1966)
2661	Observation of Interband Transitions in Cd_3As_2	E. D. Haidemenakis [†] J. G. Mavroides M. S. Dresselhaus D. F. Kolesar	Solid State Commun. <u>4</u> , 65 (1966)
2667	Four-Probe Device for Accurate Measurement of the Temperature Dependence of Electrical Resistivity on Small, Irregularly Shaped Single Crystals	R. W. Germann D. B. Rogers	Rev. Sci. Instr. <u>37</u> , 273 (1966)
2668	On the Polaron Energy Spectrum	D. M. Larsen	Phys. Rev. <u>144</u> , 697 (1966)

* Reprints available.

[†] Author not at Lincoln Laboratory.

JA No.

- 2670 Remarks on "An Explanation of the High Cation Vacancy Concentration and p-Type Conductivity in Semiconductors Containing a Multivalent Metal in Its Lowest Valence State" R. F. Brebrick J. Phys. Chem. Solids 27, 617 (1966)
- 2672 Pseudobinary InSb-InTe System A. J. Strauss M. D. Banus M. C. Finn J. Electrochem. Soc. 113, 458 (1966)
- 2731 Comparative Data on CdS Transducers from 14 Mc/s to 70 Gc/s R. Weber Proc. IEEE (Correspondence) 54, 333 (1966)
- 2757 Electron-Beam Pumped Lasers of CdSe and CdS C. E. Hurwitz Appl. Phys. Letters 8, 121 (1966)
- 2760 Polaron Induced Anomalies in the Interband Magnetoabsorption of InSb E. J. Johnson D. M. Larsen Phys. Rev. Letters 16, 655 (1966)
- 2766 Spontaneous and Coherent Photoluminescence in $\text{Cd}_x\text{Hg}_{1-x}\text{Te}$ I. Melngailis A. J. Strauss Appl. Phys. Letters 8, 179 (1966)
- 2771 Quantum Oscillations in the Ultrasonic Attenuation and Magnetic Susceptibility of InBi Y. Shapira* S. J. Williamson* S. Fischler Phys. Rev. 144, 715 (1966)

MS No.

- 1459 Ferromagnetism in CdCr_2Se_4 and CdCr_2S_4 N. Menyuk K. Dwight R. J. Arnott A. Wold* J. Appl. Phys. 37, 1387 (1966)
- 1463 Reduced Manganese Moment in Manganese Chromite K. Dwight N. Menyuk J. Feinleib A. Wold* J. Appl. Phys. 37, 962 (1966)
- 1464 Single-Crystal Growth and Properties of the Perovskites LaVO_3 and YVO_3 D. B. Rogers A. Ferretti D. H. Ridgley R. J. Arnott J. B. Goodenough J. Appl. Phys. 37, 1431 (1966)
- 1474 Temperature Variation of the Spin-Wave Dispersion Relation R. Weber P. E. Tannenwald J. Appl. Phys. 37, 1058 (1966)
- 1475 Covalency Criterion for Localized vs Collective Electrons in Oxides with the Perovskite Structure J. B. Goodenough J. Appl. Phys. 37, 1415 (1966)
- 1477 Crystallographic Study of Chromium Spinels P. M. Raccach R. J. Bouchard* A. Wold* J. Appl. Phys. 37, 1436 (1966)

* Author not at Lincoln Laboratory.

Reports

UNPUBLISHED REPORTS

Journal Articles

JA No.

2719	Partial Pressures of $\text{Te}_2(\text{g})$ in Equilibrium with $\text{Ge}_{1/2-\delta}\text{Te}_{1/2+\delta}(\text{c})$ from Optical Density Data	R. F. Brebrick	Accepted by J. Phys. Chem. Solids
2727	Photoelectron Statistics Produced by a Laser Operating Below and Above the Threshold of Oscillation	C. Freed H. A. Haus*	Accepted by IEEE J. Quant. Electron.
2739	Oscillatory Faraday Rotation of the Indirect Transition in Germanium at 1.7°K	J. Halpern	Accepted by J. Phys. Chem. Solids
2740	Phonon Generation, Propagation and Attenuation at 70 Gc	J. B. Thaxter P. E. Tannenwald	Accepted by IEEE Trans. Sonics and Ultrasonics
2747	Space-Time Symmetry Restrictions on Transport Coefficients. II. Two Theories Compared	W. H. Kleiner	Accepted by Phys. Rev.
2749	Absorption Near the Fundamental Edge	E. J. Johnson	Accepted as chapter in Vol. 3, <u>Physics of III-V Compounds</u> , R. K. Willardson and A. C. Beer, eds. (Academic Press, New York)
2762	An Electron-Bombardment Technique for the Deposition of CdS Film Transducers	R. Weber	Accepted by Rev. Sci. Instr.
2776	Efficient Visible Lasers of $\text{CdS}_x\text{Se}_{1-x}$ by Electron Beam Excitation	C. E. Hurwitz	Accepted by Appl. Phys. Letters
2802	Observation of the Interaction of Plasmons with LO Phonons in GaAs	A. Mooradian G. B. Wright	Accepted by Phys. Rev. Letters

Meeting Speeches†

MS No.

1246A	Effects of Strain on Infrared Absorption Spectra of Sulfur-Doped Silicon	W. E. Krag W. H. Kleiner H. J. Zeiger S. Fischler	} American Physical Society, Durham, North Carolina, 28-31 March 1966
1517B	On Ground Hartree-Fock States	T. A. Kaplan W. H. Kleiner	

* Author not at Lincoln Laboratory.

† Titles of Meeting Speeches are listed for information only. No copies are available for distribution.

MS No.			
1557	Oscillatory Magnetoabsorption of the Direct Transition in the Layer Compound GaSe at 1.5°K	J. Halpern	American Physical Society, Durham, North Carolina, 28-31 March 1966
1564	Homogeneity Range and Thermodynamic Properties of GeTe(c)	R. F. Brebrick	
1566	Electrical Properties and Disorder Model of GeTe	A. J. Strauss R. F. Brebrick	
1575	Optical Properties of the Metal ReO ₃ from 0.1-12 eV	J. Feinleib W. J. Scouler A. Ferretti	
1576	Interband Magnetoreflexion in HgTe	R. N. Brown* S. H. Groves	
1578	Magnetoplasma Cyclotron Resonance in PbSe	S. Bermon	
1579	Quantum Theory of Kinetic Equations for Electrons in Random Impurities	E. S. Kirkpatrick* P. N. Argyres	
1580	Magnetoacoustic Effects at 9 Gc in n-InSb	K. W. Nill A. L. McWhorter	
1581	Mass Anisotropy and Nonlocal Field Corrections to Helicon Propagation in n-PbTe	J. N. Walpole A. L. McWhorter	
1585	Lineshape Analysis of the Magneto-reflection Experiment	M. S. Dresselhaus G. F. Dresselhaus J. G. Mavroides P. R. Schroeder*	
1590	Band Structure and Electronic Properties of Europium Metal	A. J. Freeman* J. O. Dimmock	
1629	Narrow-Band Electrons in Transition-Metal Oxides	J. B. Goodenough	
1246B	The Effects of Strain on Infrared Absorption Spectra of Sulfur-Doped Silicon	W. E. Krag	
1331A	Semiconductor-to-Metal Transition in Transition Metal Oxides	J. Feinleib	Seminar, Tufts University, 13 April 1966
1492C	The Gunn Effect	A. L. McWhorter	Colloquium, Case Institute of Technology, 28 April 1966
1493	High Pressure Synthesis of Arsenopyrite-Type Ternary Compounds	M. D. Banus M. C. Lavine	AIME Annual Meeting, New York, 27 February - 3 March 1966

* Author not at Lincoln Laboratory.

Reports

MS No.

1534A	Refractive-Index Changes in Absorbing Media by a Pulsed Laser Beam	P.R. Longaker M.M. Litvak	Seminar, United Aircraft Research Laboratories, East Hartford, Connecticut, 28 April 1966
1545C	Light Beam Self-Focusing in Non-linear Media	P. L. Kelley	Colloquium, Northwestern University, 11 April 1966
1554	Spectroscopic Studies of Laser-Produced Hydrogen Plasma	M. M. Litvak D. F. Edwards*	} Fourth International Quantum Electronics Conference, Phoenix, Arizona, 12-14 April 1966
1558	Possibility of Self-Focusing Due to Nonlinear Anomalous Dispersion	A. Javan* P. L. Kelley	
1561	Electron Beam Pumped Lasers of CdS and CdSe	C. E. Hurwitz	
1567	Photoelectron Statistics Produced by a Laser Operating Below and Above the Threshold of Oscillation	C. Freed H. A. Haus*	
1594	Temperature Dependence of Incoherent Second Harmonic Light Scattering in Liquids	D. L. Weinberg	} American Physical Society, Washington, D. C., 25-28 April 1966
1661	The Fourier Expansion for Electronic Energy Bands	G. F. Dresselhaus	
1605	Theory of Excitons	J. O. Dimmock	Colloquium, Colorado State University, 18 February 1966
1617	Research in Narrow Band-Gap Lasers and the Optical and Electron-Beam Stimulation of Semiconductor Lasers	R. H. Rediker	Seminar, Stevens Institute of Technology, 11 May 1966
1627A	Semiconductor Lasers	R. H. Rediker	} Industrial Liaison Symposia, M. I. T., 28 April 1966
1645	Laser Radars	R. J. Keyes	
1631	Microwave Amplification and Gunn Oscillations in GaAs	A. L. McWhorter	Seminar, Texas Instruments, Inc., Dallas, Texas, 3 March 1966
1634	Microwave Amplification and Gunn Oscillation in Polar Semiconductors	A. G. Foyt	North American Aviation Colloquium, Thousand Oaks, California, 18 March 1966
1665	Maser Amplification of Interstellar OH Emission	M. M. Litvak A. L. McWhorter M. L. Meeks† H. J. Zeiger	URSI Spring Meeting, Washington, D. C., 19 April 1966
1673	Computer Installation Management - Small, Medium and Large	V. J. Mason	SDS Spring Conference, Boston, Massachusetts, 30 April 1966

* Author not at Lincoln Laboratory.

† Division 3.

I. SOLID STATE DEVICE RESEARCH

A. EFFICIENT VISIBLE LASERS OF $\text{CdS}_x\text{Se}_{1-x}$ BY ELECTRON BEAM EXCITATION*

Electron beam pumped laser action in CdS and CdSe has been recently reported.¹⁻⁴ In the present work, we have employed electron beam excitation on crystals of the mixed alloy $\text{CdS}_x\text{Se}_{1-x}$ to produce laser oscillations at several wavelengths from red (6900 Å) to blue (4900 Å), with up to 20 W of peak output power and as high as 11-percent power efficiency. These results, coupled with those of previous workers^{5,6} on p-n junction lasers of $\text{GaAs}_x\text{P}_{1-x}$, demonstrate that it is now possible to obtain efficient semiconductor lasers anywhere in a continuous range of wavelengths from 8400 to 4900 Å.

Laser samples were made from high-purity, single-crystal, vapor-grown platelets of seven different compositions varying from pure CdSe to pure CdS. The sample preparation and experimental technique have been described previously.³ The onset of laser action was clearly evidenced by a strong superlinear increase of emission intensity with beam current, by narrowing of the spectral line with simultaneous formation of well-defined Fabry-Perot cavity modes, and by the appearance of spatial diffraction patterns in the emitted light. In all cases, both the spontaneous and stimulated radiation were strongly polarized with $E \perp c$.

Laser emission always occurred at a wavelength within 10 Å of the peak of the 30- to 50-Å wide dominant spontaneous line, and appeared most frequently, but not exclusively, on the low-energy side. A plot of the laser photon energy and corresponding wavelength as a function of crystal composition is presented in Fig. I-1. Compositions were determined by electron microprobe analysis of samples adjacent to those from which lasers were fabricated. Since there was some scatter in the analysis data, the compositions given in Fig. I-1 and in Table I-1 are felt to be representative of the true values within about ±5 mole-percent.

From the previous results on CdS and CdSe lasers,¹⁻⁴ it is quite certain that in these materials the pertinent optical transitions involve a bound exciton-impurity complex, and presumably this is also the case in the mixed alloys, even though sharp exciton emission lines have not been observed in these crystals.⁷ In this regard, we have attempted to correlate the photon energies of Fig. I-1 with the exciton energies in $\text{CdS}_x\text{Se}_{1-x}$ crystals obtained from photoconductivity and transmission data by Park and Reynolds.⁸ We find good agreement for pure CdS and CdSe, with our results lying slightly lower in energy than the A exciton, as expected, since the latter is a free exciton.⁹ For intermediate compositions, however, the peak energies in the present results are somewhat higher than those reported for the A exciton. We attribute this to the differences in the methods employed for determining composition.

The functional behavior of the laser threshold current, output power, and efficiency with respect to beam voltage was essentially the same as that previously reported³ for CdS and CdSe

*The work described in this section was supported in part by the AF Avionics Laboratory Director's Fund, Item Nr. 65-86.

Section I

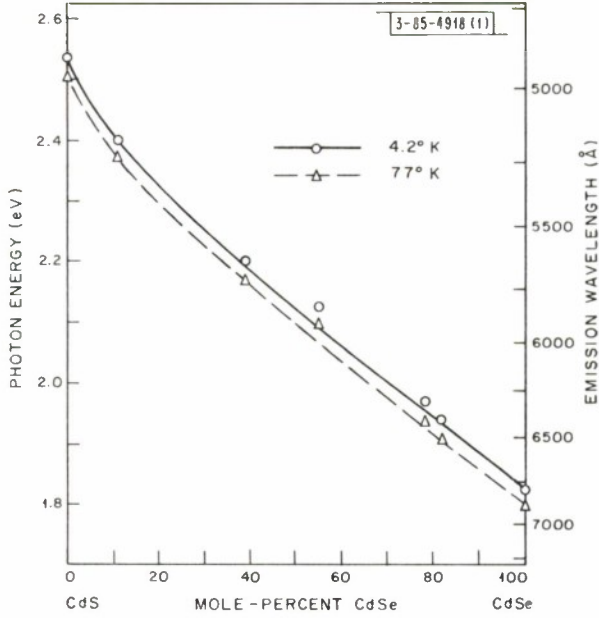


Fig. I-1. Photon energy and corresponding wavelength of CdS_xSe_{1-x} lasers at 4.2° and 77°K as function of crystal composition.

TABLE I-1			
THRESHOLD CURRENT DENSITY, PEAK OUTPUT POWER, AND MAXIMUM OBSERVED EFFICIENCY OF CdS_xSe_{1-x} LASERS AT 4.2°K (Upper Figures) AND 77°K (Lower Figures)			
Mole-Percent CdSe	Threshold Current Density (mA/cm ²)	Output Power (W)	Efficiency (percent)
0	1000	10	0.7
	1200	5	0.4
11	80	10	7
	400	6	4
39	30	20	11
	80	8	9
55	40	11	9
	400	7	5
79	120	3	3
	600	1	2
82	100	5	4
	450	3	3
100	50	16	8
	200	14	7

lasers. For 50-keV electrons, the minimum measured threshold beam current density and the maximum observed peak output power and power efficiency for lasers of the various material compositions are given in Table I-1. The results reported in the table are for sample dimensions $0.25 \times 1.5 \text{ mm} \times 4$ to 20μ and beam voltage of 50 kV. Included in the table are more recent results for the threshold current densities in CdSe. These values are substantially lower than those presented earlier.³ In fact, the threshold currents for all materials except CdS are sufficiently low that heating by the beam is minimal; consequently, the sample temperatures with coolants of liquid helium and liquid nitrogen are within a few degrees of 4.2° and 77°K , respectively, as opposed to about 40° and 100°K in the earlier measurements. As a result, there is now a significant difference in threshold current between helium and nitrogen temperatures.

The values of threshold current and efficiency varied widely between different samples of the same composition and even from point to point on the same sample. Since the samples appeared to be identical in other respects, including perfection of the cleaved cavity faces, as examined under high magnification, the variations must be attributed to inhomogeneities in some relevant bulk property of the crystals. Thus, it is not reasonable to try to establish a definite pattern of threshold and efficiency vs composition from the data of Table I-1, with the obvious exception of the anomalously high threshold and low efficiency in the pure CdS. This behavior was observed in all CdS samples from several crystals and as yet remains unexplained. The somewhat lower output power and efficiency and higher threshold of the crystals with $x = 0.1$ and 0.2 is due to the fact that these platelets were extremely thin (4 to 5μ) and a significant fraction of the incident fast electrons passed completely through the samples.

Finally, with respect to the data in Table I-1 it is important to note that the width of all samples was 0.25 mm while the beam diameter was approximately 0.5 mm . Hence, only about two-thirds of the incident electrons actually impinged on the sample, and the true efficiencies are therefore at least one and one-half times higher than the values in Table I-1. Further, since there is some backscattering of the incident electrons and the laser emission is known to occur in small filaments, the local efficiency is presumably even higher. In some cases, it may well approach 30 percent, the value sometimes quoted as the limit imposed by the energy loss inherent in the creation of electron-hole pairs by fast electrons.^{10,11}

C. E. Hurwitz

B. SPONTANEOUS AND COHERENT PHOTOLUMINESCENCE IN $\text{Cd}_x\text{Hg}_{1-x}\text{Te}$

We have observed spontaneous emission at wavelengths from 3 to 15μ and laser emission at 3.8 and 4.1μ from $\text{Cd}_x\text{Hg}_{1-x}\text{Te}$ crystals excited optically by the radiation from a GaAs diode laser. Spontaneous injection luminescence from p-n junctions has recently been observed for $\text{Cd}_{0.35}\text{Hg}_{0.65}\text{Te}$ at 3.7μ (Ref. 12) and for CdTe at about 0.85μ (Ref. 13), and laser action has been reported at 0.78μ in CdTe excited by fast electrons.¹⁴ Our results strongly suggest that it will be possible to make $\text{Cd}_x\text{Hg}_{1-x}\text{Te}$ lasers for the efficient generation of infrared radiation at wavelengths appreciably beyond 8.5μ , the maximum so far obtained from unstressed semiconductor lasers.¹⁵ In addition, the photoluminescence studies are of interest because they should assist in elucidating the band structure of the $\text{Cd}_x\text{Hg}_{1-x}\text{Te}$ alloys, particularly in the vicinity of the semimetal-to-semiconductor transition which occurs near $x = 0.2$ (Ref. 16).

Section I

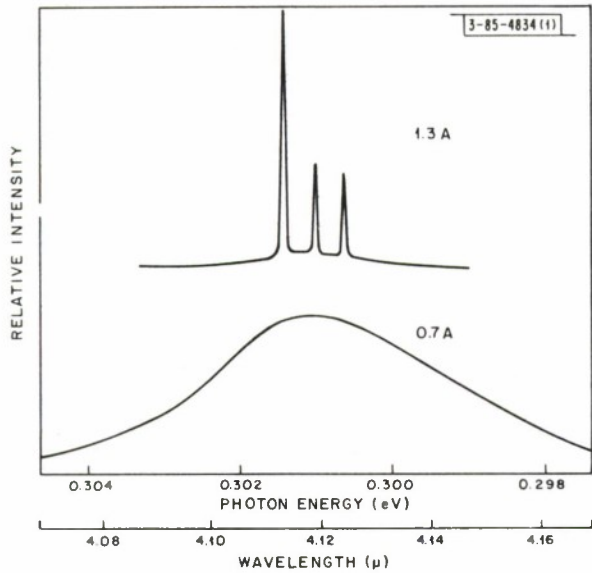
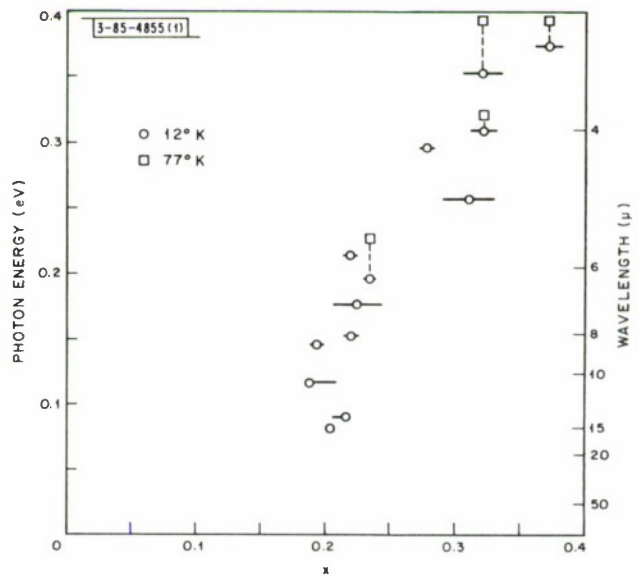


Fig. I-2. Emission spectra of optically excited $Cd_xHg_{1-x}Te$ ($x \approx 0.32$) at about $12^\circ K$ obtained below threshold at GaAs diode current of 0.7 A and above threshold at 1.3 A. Spectrum above threshold shows resolution-limited modes of 135- μ -long cavity.

Fig. I-3. Photon energy at spontaneous photoluminescence peak as function of mole fraction x of CdTe for $Cd_xHg_{1-x}Te$ samples at 12° and $77^\circ K$. Horizontal bars on experimental points indicate uncertainty in composition resulting from sample inhomogeneity.



To prepare the $\text{Cd}_x\text{Hg}_{1-x}\text{Te}$ samples, small single crystals were cut from a number of coarse-grained ingots grown by the Bridgman method. The sample surface irradiated by the GaAs laser beam was polished and etched. In the laser structures, this surface was a (110) plane, and two parallel cleaved faces perpendicular to this plane formed the Fabry-Perot cavity. The sample thickness was about $25\ \mu$, and the cavity length was typically 120 to $150\ \mu$. In all cases, the $\text{Cd}_x\text{Hg}_{1-x}\text{Te}$ sample and the GaAs laser pump were mounted on a copper heat sink which was in contact with liquid helium or nitrogen. The experimental arrangement was similar to the one previously used for optically pumping InSb lasers.¹⁷ Current pulses of a few micro-seconds duration were applied to the GaAs diode at the rate of 3000/sec.

Figure 1-2 shows emission spectra of a $\text{Cd}_x\text{Hg}_{1-x}\text{Te}$ ($x \approx 0.32$) laser at 12°K , below and above the laser threshold. The onset of coherent emission, which was evidenced by an abrupt increase in emission intensity as well as by the appearance of mode structure, occurred at a GaAs diode current of about 1 A, which corresponds to approximately 0.3 W of $0.84\text{-}\mu$ radiation. An equivalent threshold current of about 50 mA is estimated if it is assumed that one electron-hole pair is produced by each photon which is absorbed by the sample. Similar results were obtained for another $\text{Cd}_x\text{Hg}_{1-x}\text{Te}$ laser at $3.8\ \mu$. The equivalent threshold currents are considerably lower than those observed in optically pumped InSb¹⁷ and InAs¹⁸ lasers.

The mode spacing in Fig. 1-2 corresponds to a value of 5.5 for the quantity $[n_o - \lambda_o \text{ dn/d}\lambda]$ in the $135\text{-}\mu$ -long cavity. A value of 4.1 for the refractive index of $\text{Cd}_{0.14}\text{Hg}_{0.86}\text{Te}$ between 16 and $22\ \mu$ has been determined¹⁹ from the spacing of transmission interference fringes.

Spontaneous emission was obtained from $\text{Cd}_x\text{Hg}_{1-x}\text{Te}$ samples with values of x between 0.18 and 0.37. Figure 1-3 shows the photon energy at the peak of the spontaneous emission line as a function of composition, for samples at 12° and 77°K . The compositions were determined by electron probe microanalysis. Within the scatter of the data, the results agree with those previously obtained for a few samples from experiments on junction luminescence¹² at 77°K and on photovoltaic effect¹² and optical absorption²⁰ at 77° and 300°K . The decrease of peak emission energy with decreasing Cd content is due to the decrease in energy gap from semiconducting CdTe ($E_g = 1.6\ \text{eV}$ at 4.2°K) to semimetallic^{16,21} HgTe, although a sample's energy gap may be somewhat different from its peak emission energy. For $x < 0.24$, there appears to be a rather rapid decrease in peak emission energy with decreasing x , which would be consistent with a previous estimate¹⁶ that the semiconductor-to-semimetal transition occurs near $x = 0.20$.

The increase in peak emission energy between 12° and 77°K shown in Fig. 1-3, like the results of optical absorption,²⁰ photoconductivity,²² and photovoltaic¹² measurements at 77° and 300°K , is consistent with a positive temperature coefficient for the energy gap of $\text{Cd}_x\text{Hg}_{1-x}\text{Te}$ alloys with sufficiently small values of x .

I. Melngailis
A. J. Strauss

C. INCOHERENT SOURCE OPTICAL PUMPING OF VISIBLE AND INFRARED SEMICONDUCTOR LASERS

Previously, optical pumping of semiconductor lasers has required the use of another laser to obtain sufficient power densities. We report here the successful pumping of InSb and CdSe lasers at liquid helium temperature using a pulsed xenon flashlamp. This demonstrates that it

Section I

is possible to achieve laser emission from semiconductors in the infrared and visible spectral regions using an incoherent optical pump.

Optical pumping of semiconductor lasers was first achieved using GaAs diode lasers.^{23,24} Extension into the visible region was achieved by two-photon pumping of CdS using high-power ruby lasers.²⁵ At this time, the shortest wavelength which has been achieved using a diode laser pump is at the red end of the visible region. Also, the overall efficiency and required powers of the two-photon process limit its usefulness. Direct flashlamp pumping is simple, extends the short wavelength limit available using diode lasers, and avoids the limitations of an intermediate laser regarding pulse length and power. It is therefore evident that the capabilities of semiconductor lasers can be considerably extended by using a flashlamp source as an optical pump.

Although the emission of continuously operated xenon lamps peaks in the region of 0.8 to 1.0 μ , the spectra of lamps pulsed to high-current densities are shifted to the ultraviolet.²⁶ Using this shift, peak power densities in the wavelength interval of 0.6 to 0.2 μ of 15 kW cm⁻² are obtainable with but an f/1.5 one-to-one imaging system; 47 percent of this power is in the region between 0.4 and 0.2 μ . Since heating the samples can quench the laser emission, the flashlamp was turned on rapidly. The threshold power density for CdSe was obtained in 0.5 μ sec.

To decrease the required pump power densities, very thin samples were used. By making the sample thickness comparable to or less than the diffusion length, losses in the material were reduced and a greater excess carrier density was obtained for a given incident power density.²⁷ The thickness of the InSb samples was reduced to 25 to 50 μ . The CdSe samples were in the neighborhood of 10 μ thick as grown by D. C. Reynolds at Aerospace Research Laboratory, Wright-Patterson Air Force Base.

The evidence for laser emission includes all the usual observed phenomena of line narrowing, clearly defined thresholds, and well-defined beam angles. In the case of the infrared emission at 5.3 μ from InSb, we obtained detailed mode structure, threshold power densities of about 700 W cm⁻² with a 500- μ cavity, and beam angles as low as 10°. Pulse lengths for the InSb laser radiation have thus far been limited only by the length of the pump pulse. Because of thermal transients and narrow spacing, the mode structure in CdSe emitting at 0.685 μ is more difficult to obtain.²⁸ For a 250- μ cavity length, the observed emission narrowed from a spontaneous line about 50 Å wide to a stimulated emission line 4 Å wide, which is approximately the width of the envelope of the modes observed by Hurwitz²⁸ for approximately the same cavity length. Well-defined thresholds of about 4 kW cm⁻² for a 500- μ cavity and beam angles in the range of 10° to 30° were observed. In the case of the CdSe visible emission, the laser action was observed to occur in brilliant filaments that suddenly emerged at threshold. The CdSe laser pulses have thus far lasted only 0.3 μ sec and are then quenched due to self-heating.

These preliminary investigations have been limited to sample sizes common in injection and electron beam pumped lasers for comparison with previous work. However, there is no obvious size limitation with flashlamp pumping. Electron beam pumping of CdSe-CdS mixtures²⁹ has shown that laser action can be achieved throughout essentially the whole visible spectrum with high efficiencies. The ultraviolet radiation from xenon flashlamps should allow one to optically pump large scale semiconductor lasers over the whole visible spectrum.

R. J. Phelan, Jr.

D. Pb SALT DIODE LASERS

Power output, efficiency, and spatial distribution of coherent emission from recently fabricated PbS and PbSe diode lasers have been measured at diode temperatures of about 7°K. A peak power of 24 mW at 2 A with 2- μ sec current pulses was measured for PbS. This corresponds to an external quantum efficiency of about 4 percent. The CW power output at 0.6 A was 2 mW. For PbSe, a peak power of 3 mW at 2 A (2- μ sec pulses), corresponding to an external quantum efficiency of 1 percent, and a CW power output of 0.2 mW at 0.8 A were measured. In both PbS and PbSe, the spatial distribution of the coherent emission was that expected from an emitting area approximately 170 μ wide and 15 μ high, with the long dimension parallel to the junction plane. Diode end faces were about 250 μ wide.

J. F. Butler

E. PREPARATION OF HIGH-PURITY EPITAXIAL GaAs

Vapor transport processes for the growth of high-purity GaAs have an advantage over melt-growth techniques in that the lower epitaxial deposition temperatures allow for less contamination from the silica containers. The vapor-growth process that appears most promising for the preparation of high-purity GaAs utilizes Ga and AsCl₃ as the starting materials since they are commercially available with a relatively high degree of purity. For example, Knight, Effer, and Evans³⁰ have reported electron mobilities as high as 40,000 cm²/V-sec at 60°K in epitaxial layers prepared with this process, while Mehal and Cronin³¹ have obtained mobilities up to 54,000 cm²/V-sec at 77°K in a similar system. Recently, Whitaker and Bolger³² have measured mobilities reaching 101,000 cm²/V-sec at 78°K and 8500 cm²/V-sec at room temperature with carrier concentrations in the range 10¹⁴ to 10¹⁵ cm⁻³. Here we report results obtained in this Laboratory using a similar process.

The epitaxial layers are prepared in an open-tube flow system utilizing a two-zone furnace with Ga placed in the high-temperature zone (850 to 900°C) and the GaAs seeds inserted into the lower temperature (700 to 750°C) deposition region. Pure H₂ from a palladium-alloy diffuser is bubbled through the AsCl₃ at a rate of 50 to 100 ml/min, and the resultant gas mixture is passed through the furnace tube where it reacts with the Ga and deposits GaAs in the lower temperature region.

The seeds are cut to the desired orientation from Czochralski-grown crystals and chemically polished to remove saw damage. Just before use, the seeds are re-etched, soaked in a 10-percent KCN solution to complex any Cu ions adsorbed from the acid solution, rinsed in high-purity water, and inserted into the reaction tube. The tube is then flushed with Ar, and H₂ is introduced and maintained during the furnace heat-up time. To ensure a clean surface for epitaxial growth, the gas mixture is passed over the seeds at a temperature of about 900°C. After this etch, the furnace is lowered to the growth temperature where epitaxial deposition occurs at a rate of about 0.5 μ /min.

For electrical evaluation, layers are deposited on Cr-doped ($\rho > 10^7$ ohm-cm) substrates. Resistivity and Hall measurements for representative samples grown on (111) seeds are listed in Table I-2.

Free carrier concentrations are up to two orders of magnitude lower than are concentrations ordinarily obtained in melt-grown material, and up to an order of magnitude lower than

TABLE I-2
RESULTS OF RESISTIVITY AND HALL MEASUREMENTS
FOR REPRESENTATIVE SAMPLES

Run No.	300°K			77°K		
	ρ (ohm-cm)	n (cm ⁻³)	μ (cm ² /V-sec)	ρ (ohm-cm)	n (cm ⁻³)	μ (cm ² /V-sec)
039-2	1.2	8.9×10^{14}	5900	0.16	7.2×10^{14}	54,000
039-3	2.0	5.2×10^{14}	6200	0.33	4.6×10^{14}	41,000
042-2	0.68	1.2×10^{15}	8000	0.10	1.2×10^{15}	54,000
043-1	1.2	7.3×10^{14}	7200	0.12	7.3×10^{14}	70,000
043-2	0.42	2.0×10^{15}	7200	0.073	2.0×10^{15}	42,000
043-3	1.3	6.7×10^{14}	7200	0.16	7.2×10^{14}	56,000

concentrations obtained with other vapor-growth systems. Similar results have been obtained by other workers.³⁰⁻³² Some idea of the amount of compensation in this material can be obtained by examining the mobilities at liquid nitrogen temperature where ionized impurity scattering is dominant.³³ Run No. 043-1, for example, has a free carrier density $N_D - N_A = 7.3 \times 10^{14}$ cm⁻³, and a mobility $\mu = 70,000$ cm²/V-sec. Taking into account the effects of polar mode scattering and the screening of ionized impurities by free carriers, a total ionized impurity density $N_D + N_A$ of 1.9×10^{15} cm⁻³ is obtained for this material at liquid nitrogen temperature.

Several problems which have been encountered in the epitaxial growth of high-purity GaAs should be mentioned. Hillock formation and rather high stacking fault densities have been observed. In addition, there has been some difficulty in obtaining a smooth thermally etched surface, resulting in a rough interface between the substrate and the epitaxial layer.

C. M. Wolfe
T. M. Quist
A. J. Strauss

REFERENCES

1. N.G. Basov, O.V. Bogdankevich, and A.G. Devyatkov, *Doklady Akad. Nauk S.S.S.R.* 155, 783 (1964) [English translation: *Soviet Phys. – Doklady* 9, 788 (1964)]; N.G. Basov, *Physics of Quantum Electronics Conference Proceedings, 1965* (McGraw-Hill, New York, 1966), p.411.
2. C. Benoit à la Guillaume and J.M. Dehever, *Compt. rend.* 261, 5428 (1965).
3. C.E. Hurwitz, *Appl. Phys. Letters* 8, 121 (1966). and references cited therein; *Solid State Research Report*, Lincoln Laboratory, M.I.T. (1966:1), p. 1, DDC 632998, H-721.
4. E.L. Nolle, V.S. Vavilov, G.P. Golubev, and V.S. Mashtakov, *Fiz. Tverd. Tela* 8, 286 (1966).
5. N. Holonyak, Jr., and S. Bevaqua, *Appl. Phys. Letters* 2, 176 (1963); N. Holonyak, Jr., *Trans. Met. Soc. AIME* 230, 276 (1964).
6. M. Pilkuhn and H. Rupprecht, *J. Appl. Phys.* 36, 684 (1965).
7. D.C. Reynolds, private communication.
8. Y.S. Park and D.C. Reynolds, *Phys. Rev.* 132, 2459 (1963).
9. D.C. Reynolds, C.W. Litton, and T.C. Collins, *Phys. Stat. Sol.* 9, 645 (1965); 12, 3 (1965).
10. W. Shockley, *Czech. J. Phys.* B11, 81 (1961).
11. V.L. Levshin, *et al.*, *Soviet Researches on Luminescence*, edited by D.V. Skobel'tsyn (Consultants Bureau, New York, 1964), pp.62-69.
12. C. Verié and R. Granger, *Compt. rend.* 261, 3349 (1965).
13. G. Mandel and F.F. Morehead, *Appl. Phys. Letters* 4, 143 (1964).
14. V.S. Vavilov and E.L. Nolle, *Doklady Akad. Nauk S.S.S.R.* 164, 73 (1965).
15. J.F. Butler, *et al.*, *Solid State Commun.* 2, 303 (1964), DDC 453105.
16. A.J. Strauss, *et al.*, *Proceedings of the International Conference on Semiconductor Physics, Exeter, 1962* (Institute of Physics and the Physical Society, London, 1962), p.703; T.C. Harman, *et al.*, *Solid State Commun.* 2, 305 (1964), DDC 453102.
17. R.J. Phelan, Jr., and R.H. Rediker, *Appl. Phys. Letters* 6, 70 (1965), DDC 613905.
18. I. Melngailis, *IEEE J. Quant. Electron.* QE-1, 104 (1965), DDC 621208.
19. T.C. Harman, *et al.*, *Phys. Rev. Letters* 7, 403 (1961).
20. M.D. Blue, *Phys. Rev.* 134, A226 (1964).
21. H. Rodot, M. Rodot, and R. Trihoulet, *Compt. rend.* 256, 5535 (1963).
22. P.W. Kruse, *Appl. Optics* 4, 687 (1965).
23. R.J. Phelan, Jr., and R.H. Rediker, *Appl. Phys. Letters* 6, 70 (1965), DDC 613905.
24. I. Melngailis, *IEEE J. Quant. Electron.* QE-1, 104 (1965), DDC 621208.
25. N.G. Basov, A. Z. Grasyuk, I. G. Zubarev, and V. A. Katulin, *Fiz. Tverd. Tela* 7, 3640 (1965).
26. J.H. Gonca and P.B. Newell, *J. Opt. Soc. Am.* 56, 87 (1966).
27. R.J. Phelan, Jr., *Physics of Quantum Electronics* (McGraw-Hill, New York, 1966), p.435.
28. C.E. Hurwitz, *Appl. Phys. Letters* 8, 121 (1966).
29. _____, to be published in *Appl. Phys. Letters*.
30. J.R. Knight, D. Effer, and P.R. Evans, *Solid-State Electron.* 8, 178 (1965).
31. E.W. Mehal and G.R. Cronin, to be published in *Electrochemical Technology*.
32. J. Whitaker and D.E. Bolger, *Solid State Commun.* 4, 181 (1966).
33. H. Ehrenreich, *Phys. Rev.* 120, 1951 (1960).

II. OPTICAL TECHNIQUES AND DEVICES

A. PHOTOELECTRON STATISTICS PRODUCED BY LASER ABOVE THRESHOLD OF OSCILLATION

Laser light above but near threshold is adequately represented by a probability distribution of the intensity that peaks near the average intensity and has a small spread due to the modulation. The probability distribution for this case has been analyzed by Glauber,¹ who obtained the results given in Eqs. (1) and (2) for the probability distribution and the factorial moments of photoelectrons, respectively.

$$P(n) = \frac{(\langle C \rangle_N)^n}{(1 + \langle C \rangle_N)^{n+1}} L_n \left[\frac{\langle C \rangle_S}{\langle C \rangle_N (1 + \langle C \rangle_N)} \right] \exp \left[- \frac{\langle C \rangle_S}{1 + \langle C \rangle_N} \right] \quad (1)$$

$$\left\langle \frac{C!}{(C-n)!} \right\rangle = n! (\langle C \rangle_N)^n L_n \left[- \frac{\langle C \rangle_S}{\langle C \rangle_N} \right] \quad (2)$$

where $\langle C \rangle_S$ and $\langle C \rangle_N$ represent the mean number of quanta which would be counted in the coherent (signal) field and the noise field, respectively, if each of these fields were the only one present (L_n denotes the normalized Laguerre polynomials).

When the strength of the coherent signal goes to zero, the probability distribution reduces to the familiar power law given by the first factor of Eq. (1). When the noise signal vanishes, the Poisson distribution characteristics of coherent fields emerge.

Figures II-1(a) through (c) show the experimentally determined probability distribution $P(n)$ and the number of samples observed $S(n)$ for a given length of counting interval. The vertical bars indicate the predicted spread of data and are proportional to the square root of the number of samples taken. These results were obtained with the laser operating above the threshold of oscillation. An ideal laser with no fluctuations should produce a pure Poisson probability distribution. For comparison, the applicable Poisson curves are shown as dashed lines. It can be seen that the observed distributions are somewhat wider than the ideal Poisson distribution. This can be attributed to modulation of the light, a case to which Eq. (1) applies. The values of $\langle C \rangle_S$ and $\langle C \rangle_N$ utilized in computing the theoretical curves shown by solid lines in Figs. II-1(a) to (c) were evaluated from the experimentally obtained data for \bar{n} , \bar{n}^2 , and Eq. (2). These theoretical curves represented the best fit to our experimental data in the sense that, trying a least-square-error approximation, no better solution could be found within at least three significant figures.

Figure II-1(a) represents data taken nearest to threshold of the laser oscillator. At this operating point, the output power was approximately 50 times greater than measured for the laser operating at the same bandwidth but below the threshold of oscillation. Above the threshold of oscillation, we may define the modulation as

$$m = \sqrt{\frac{\langle C \rangle_N}{\langle C \rangle_S}} \quad .$$

Section II

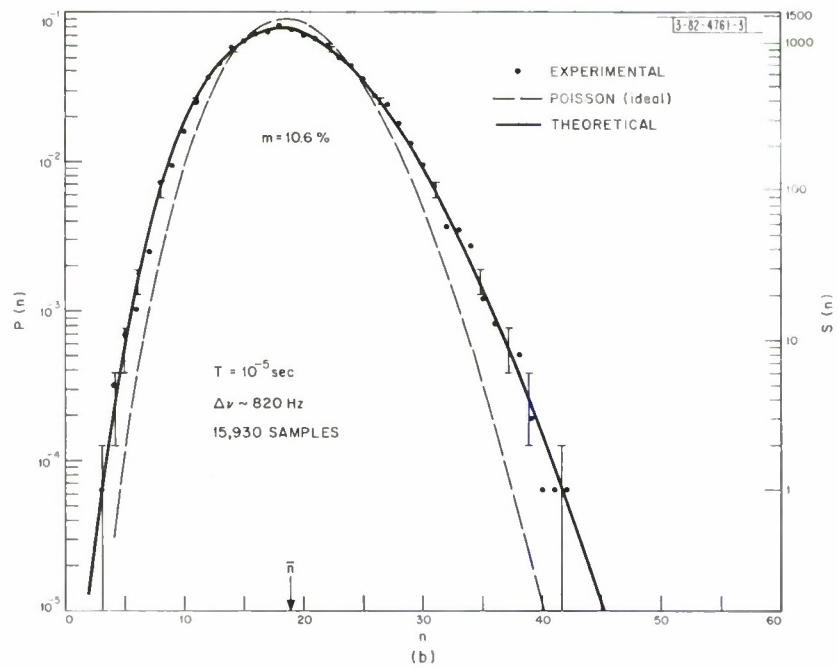
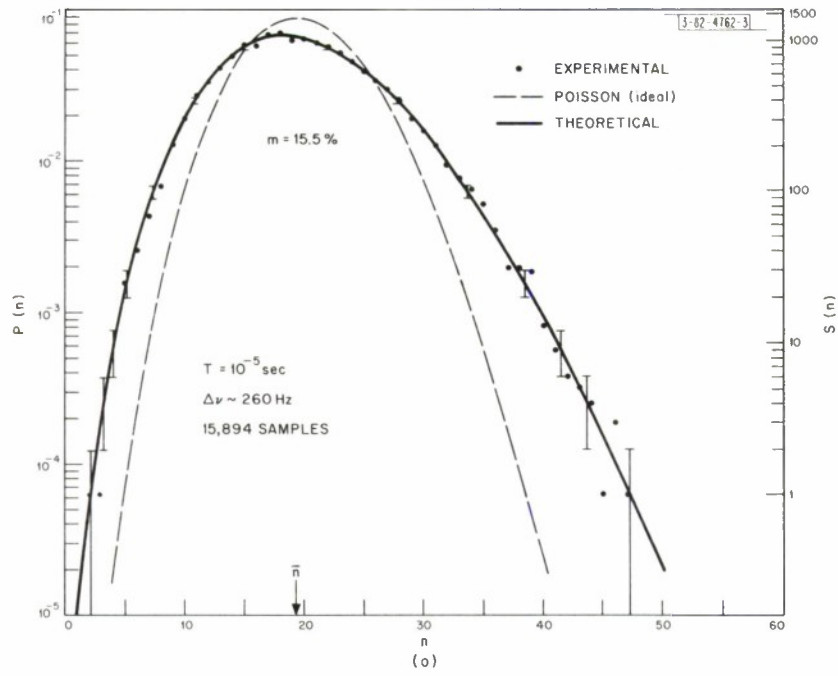


Fig. II-1(o-c). Probability distribution and number of observed samples vs photoelectron count above threshold.

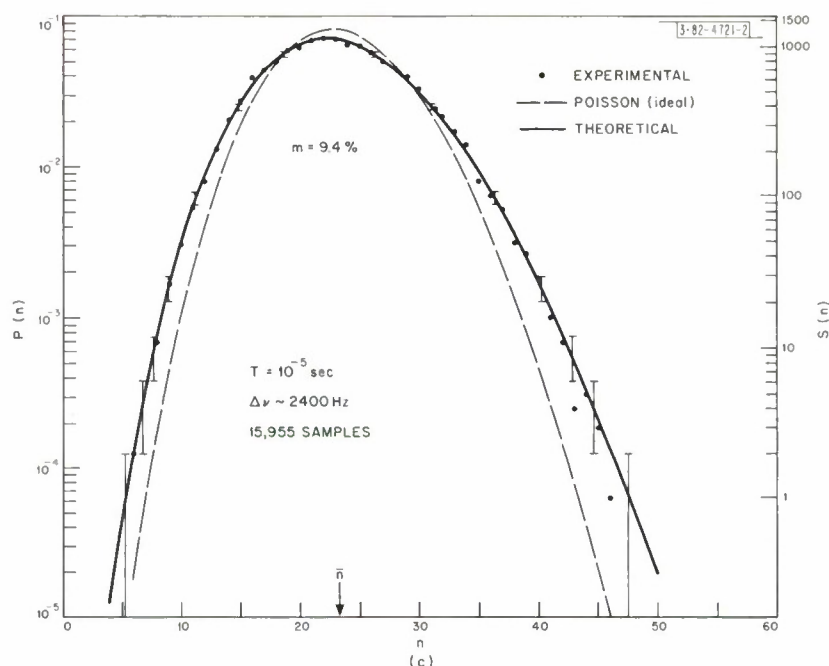


Fig. II-1. Continued.

Let us assume that the modulation m on each of Figs. II-1(a) to (c) resulted from a combination of spontaneous emission noise modulation m_ν and a residual modulation m_r which almost inevitably arose during the data-taking process because of slow random drifts and changes in quantum efficiencies, detector gains, reference voltages and resistances, temperatures, feedback effects, etc. Furthermore, it is reasonable to assume that m_r arose from random processes which were statistically independent of spontaneous noise modulation and remained constant during the few hours it took to accumulate these data. We have previously shown that m_ν decreases inversely proportional to power or bandwidth near and above the threshold as expected from the van der Pol theory of oscillators.² We may then compute the different modulations as indicated in Table II-1 and use the bandwidths (measured on a spectrum analyzer) as an additional check of the results. Table II-1 gives a summary of some of the data pertinent to Figs. II-1(a) to (c). The result

TABLE II-1				
Power (μ W)	$\Delta\nu$ (Hz)	Total Modulation m (percent)	Residual Modulation m_r (percent)	Spontaneous Emission Modulation m_ν (percent)
0.27	2400	9.4	9.2	1.7
0.086	820	10.6	9.2	5.1
0.029	260	15.5	9.2	12.4
$m^2 \approx m_r^2 + m_\nu^2$				

Section II

indicates a residual modulation of the order of 9 percent, and an agreement well within the accuracy of our spectral and power measurements.

C. Freed
H. A. Haus*

B. DETECTABILITY OF Cu-DOPED GERMANIUM

By using very pure host crystals in which the donor concentration is less than $3 \times 10^{13}/\text{cm}^3$, it has been possible to produce far infrared detectors which are photon-induced g-r noise limited down to a background photon flux of 3×10^{11} photons/sec. The unique characteristic of these detectors is the relatively long lifetime of the excited holes, which is a direct result of the reduction of the residual donor impurities in the host material prior to copper diffusion. Long free carrier lifetimes increase the internal gain of the photoconductor ($G = \text{hole current}/\text{photon flux}$) to a level such that the photon-induced noise is greater than that of the preamplifier.

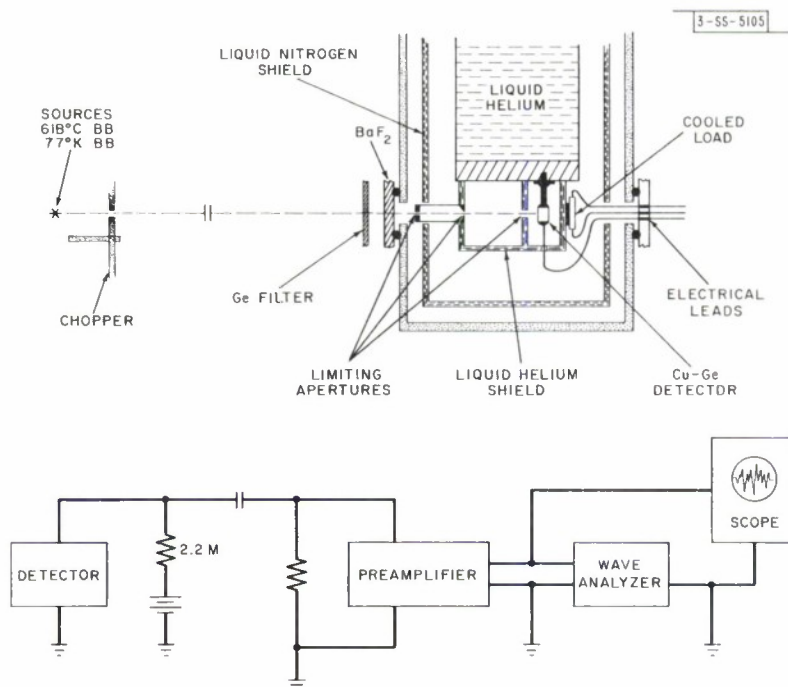


Fig. II-2. Diagram of test setup and electrical measuring circuit.

The detectors, 3-mm cubes, were cut from a 2-cm-diameter wafer into which approximately 6×10^{15} copper atoms/cm³ were indiffused³ for a period of 16 hours. The host crystals contained 3×10^{13} donor centers which produced detectors with a free hole lifetime of 5×10^{-8} sec. The best results in terms of noise-free contacts at liquid helium temperature were obtained with Cerroseal soldered contacts to opposite faces of the sensor. Pure indium alloyed contacts seemed less reproducible and more noisy in spite of the normal advantages of that technique. One 20-mil

* Department of Electrical Engineering and Research Laboratory of Electronics, M.I.T.

heavy gold wire soldered directly to the Cerroal served both as an electrical connection and as a heat flow path to the liquid helium heat sink. Figure II-2 is a schematic drawing of the test setup, including a diagram of the electrical measuring apparatus. It should be noted that (1) the cold shields are directly attached to the helium finger. Since a background flux of 3×10^{11} photons/sec is equivalent to looking into a cavity at approximately 36°K, it is important that the cavity be kept at a temperature lower than 36°K. (2) The 2.2-megohm metal film resistor is also attached to the helium cold finger via thermal conducting cement in order to reduce the thermal noise of the load resistor. A calibrated Perkin-Elmer blackbody at 618°C, 130 cm from the detector entrance aperture, was used as a calibrated source for the 4- μ spectral region. The chopper blades at 300°K served as a 10- μ radiation source when a 77°K background was placed behind them. Both sources yielded the same NEP for the detectors after a correction for the λ distribution difference was made. The DC current in the sample along with the responsivity obtained from the calibrated sources gave a cross check on the calculation of the average background flux level. The relative signal and detector noise voltages as well as the S/N ratio as a function of the voltage applied to the sensor for a background flux of 3×10^{11} photons/sec are plotted in Fig. II-3. Beyond 25 V, corresponding to an electric field of 83 V/cm, the noise increased faster than the signal. Below this voltage, the S/N ratio was constant yielding a

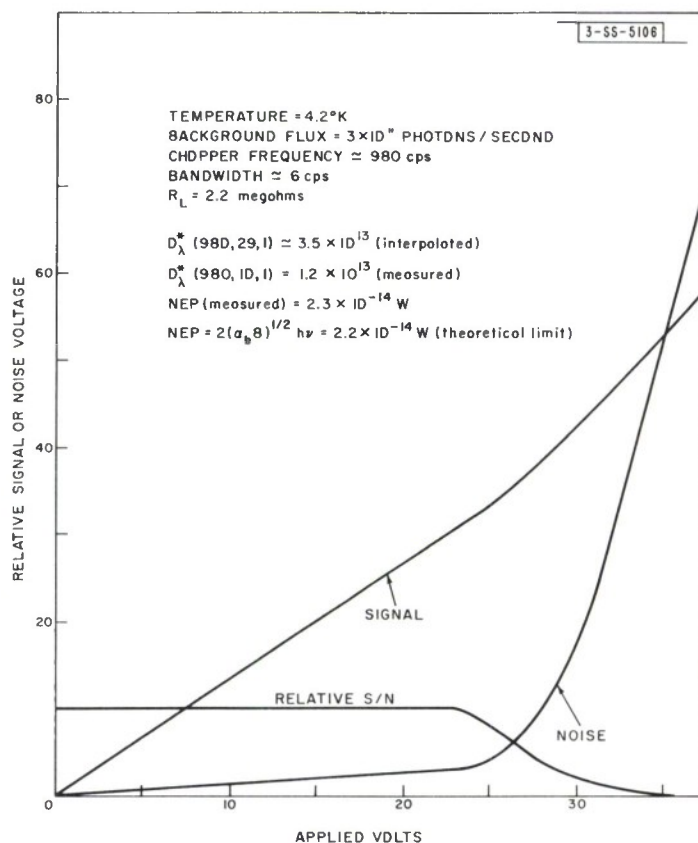


Fig. II-3. Relative signal, noise, and S/N as function of applied voltage of Cu-doped Ge detector.

Section II

measured NEP of 2.5×10^{-14} W at 10μ which, within the accuracy of our measurements, agrees with the theoretical photon-generated g-r noise limit of

$$2(\alpha_b B)^{1/2} h\nu = 2.2 \times 10^{-14} \text{ W}$$

where α_b is the background photon flux absorbed by the sensor. The measured NEP was independent of chopper frequency in our measurement range of 200 to 1000 Hz.

Discussion

Assuming that noiseless contacts can be made, it then seems probable that Cu-doped Ge is intrinsically capable of performing as a background limited detector down to even lower background fluxes than our measurements entailed. Unfortunately, amplifiers have a noise voltage of their own, and the problem of detecting photon-induced noise at much lower background levels is basically a problem of obtaining sufficient noiseless gain in the sensor to overcome preamplifier noise. Photomultiplier tubes achieve this very well by having internal gains of the order of 10^6 . The usable gain in a photoconductor to a first approximation can be expressed as

$$G = \frac{E_c \mu_p \tau}{d} = \frac{E_c \mu_p}{N_d \sigma_p v_p d}$$

where E_c is the maximum electric field that can be impressed across the detector and still maintain low noise, μ_p is the hole mobility (2×10^4 cm²/V-sec), σ_p is the capture cross section of an excited hole (approximately 10^{-13} cm²), v_p is the velocity of the free hole, d is the contact separation, and N_d is the density of donor impurities in the crystal which act indirectly as recombination sites for the free holes. Unfortunately, when N_d is reduced much below the value of 3×10^{13} /cc, the maximum field that can be impressed upon the sample is reduced and no further appreciable gain can be obtained by a reduction in N_d . The maximum low-noise gain for $d = 0.3$ was 0.25. Gains two orders higher than this were observed, but the S/N ratio was considerably less than ideal. In conclusion, it should be emphasized that the photon noise limitations have been observed to very low photon fluxes. The limit of detectability seems to lie in the preamplifiers rather than in the inherent noise of the semiconductor detector. For any frequency response, there is an optimum compensating donor concentration which will produce both the desired speed of response and the maximum gain in the Cu-doped detector.

J. H. Dennis
R. J. Keyes

C. ARGON LASER DISCHARGE ANOMALIES

The electron density measurements from Stark linewidths of argon emission have been described in a previous report.⁴ More recently, a theoretical model of the discharge has been developed that explains the anomalous behavior of the discharge and of the light emission. New data, taken for different values of axial magnetic field, exhibit the same unusual dependence on current that had been reported for the spontaneously emitted 4880-Å radiation and the sustaining voltage. The laser threshold for this tube in the range of pressure and magnetic field used is above the current where the dip occurred in the other measured quantities. Figure II-4 shows

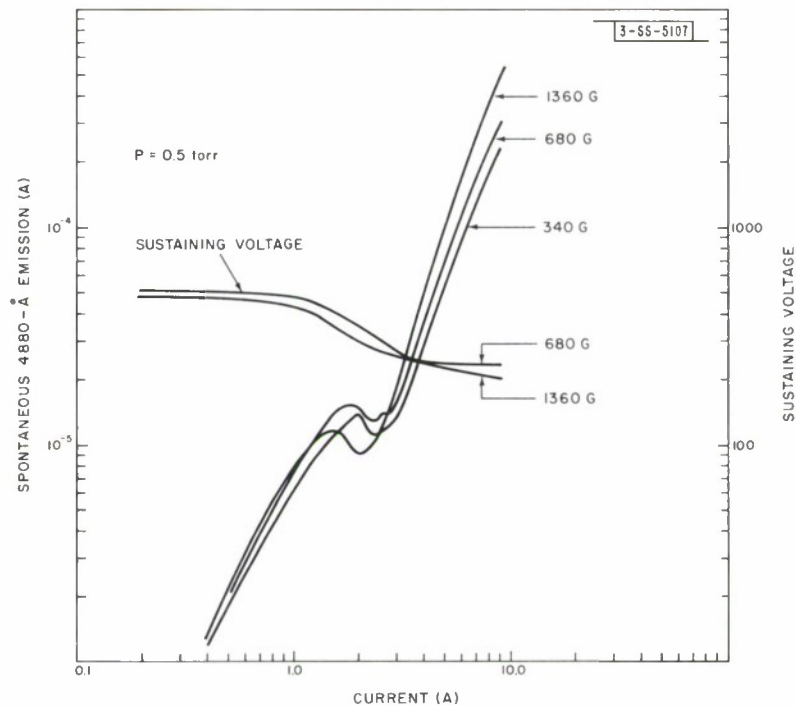


Fig. II-4. Spontaneous emission of 4880 Å (a laser transition) and sustaining voltage across discharge tube as functions of current, at pressure of 0.5 torr, for 340-, 680-, and 1360-G axial magnetic field.

a representative family of curves for different values of axial magnetic field. The 340-G curve is very similar to that for zero field, which is not shown. As expected, the 4880-Å emission increases and the sustaining voltage decreases with increasing magnetic field, as the electron concentration is increased at the tube axis. The dip in the spontaneous emission and the drop of sustaining voltage occur at lower currents with increasing magnetic field. Other data indicate that the dip in the curves becomes more pronounced at higher than 0.5-torr pressure and occurs at higher current. While at a pressure of only 0.15 torr, the dip in the spontaneous emission is replaced by a flattening of the curve. This behavior with pressure and magnetic field indicates that the anomalies occur when the electron pressure, which is proportional to electron density and temperature, becomes comparable to the neutral atom pressure.

The experimental results are predicted from a model of the constricted discharge in which a hot, highly conducting core is surrounded by a lower conductivity annular region bounded by the tube wall. The ions have a charge-exchange mean free path of the order of the tube radius when the neutral gas density is reduced because of heating by the high current. Then, there is nearly free fall of electrons and ions in the central region and, therefore, the current density and electron number density are nearly constant with radius in the central portion of the tube. In the annular region outside the core, the electron density approaches zero at the wall and the dominant electron collisions are with atoms, rather than with ions, as in the core. Ordinary ambipolar diffusion limits the charged particle flux through the annular region. The main loss term in the energy balance equation is assumed to be the ionization energy deposited at the walls.

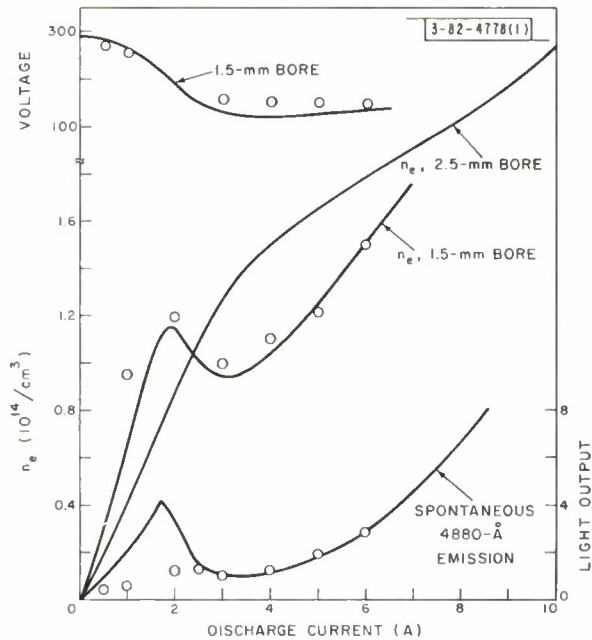


Fig. II-5. Electron density (obtained from Stark line-widths), spontaneous emission at 4880 Å, and sustaining voltage, for 0.75-torr pressure, as functions of discharge current.

The ambipolar diffusion equation, together with the energy balance and the condition of a uniform axial electric field with radius, then predict an electron density profile, ionization rate, and core radius. A simple Bessel eigenfunction solution of the diffusion equation in the annulus is matched to the solution for the case of free-fall flux out of the core. The resulting electron densities at the tube center agree reasonably well with the data. The voltage drop and the electron temperature (3 to 4 eV) are obtained from the calculated eigenvalue ionization rate. The emission of radiation is predicted from a two-step electron collision process and a Maxwellian electron distribution for the moderately high currents. The absence of a peak in the emission data might be due to the prevalence of one-step over two-step excitation for the lower currents. Figure II-5 shows the theoretical curves for the discharge parameters compared to the experimental data (shown as open circles). The anomalies are shown to result from a transition from ambipolar diffusion to free-fall ion motion when the electron pressure at the tube axis is appreciable.

R. J. Carbone
M. M. Litvak

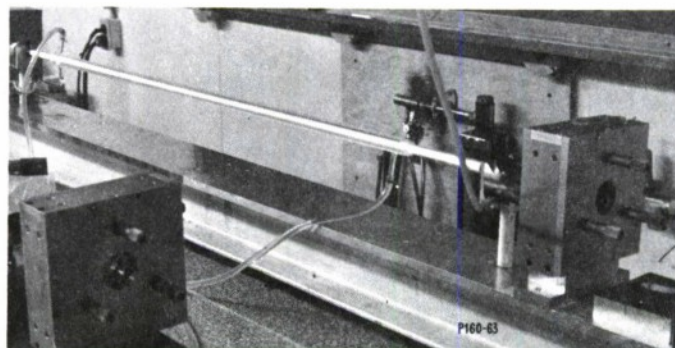


Fig. II-6. Single-mode 10.6- μ CO₂ laser with Brewster windows in 154-cm cavity.

D. SINGLE-MODE CO₂ LASER AT 10.6 μ

A sealed-off, 10-W, single-mode (axial and transverse TEM_{00q}) laser has been constructed that has an optical-to-electrical efficiency of 7 percent with the laser cavity tuned to a single line output. The laser is shown in Fig. II-6. The water-jacketed tube has a bore of 10 mm, an active medium length of 1.2 meters, and a mirror separation of 1.54 meters. One mirror has a 2-meter radius and is gold coated for maximum reflection at 10.6 μ, and the other mirror is a flat Irtran II substrate with a multiple layer dielectric coating that has a nearly optimum transmission of 13 percent at 10.6 μ. Figure II-7 shows a plot of the laser output as measured by a monochromator with adequate dispersion to resolve adjacent rotational lines. These lines could be seen when the cavity was appropriately adjusted but, in the case shown, the mirrors were fixed so that only one line was lasing. The spot size is also shown in this figure as crudely measured on thermally sensitive paper, and as shown agrees fairly well with the computed spot size for this cavity assuming a TEM_{00q} mode. An intensity plot of the output beam was made by sampling the beam with a small-aperture detector. A topographic mapping of the beam showed a smooth Gaussian intensity variation with radius. The tube operated close to optimum output for 4 to 8 hours and then slowly degraded to 50 percent of the starting power. We feel that the lessening of power output with time is due to atmospheric leaks into the tube by the O-ring seals holding the NaCl Brewster windows in place, and to a lesser extent to chemical changes in the gas fill during operation.

R. J. Carbonc

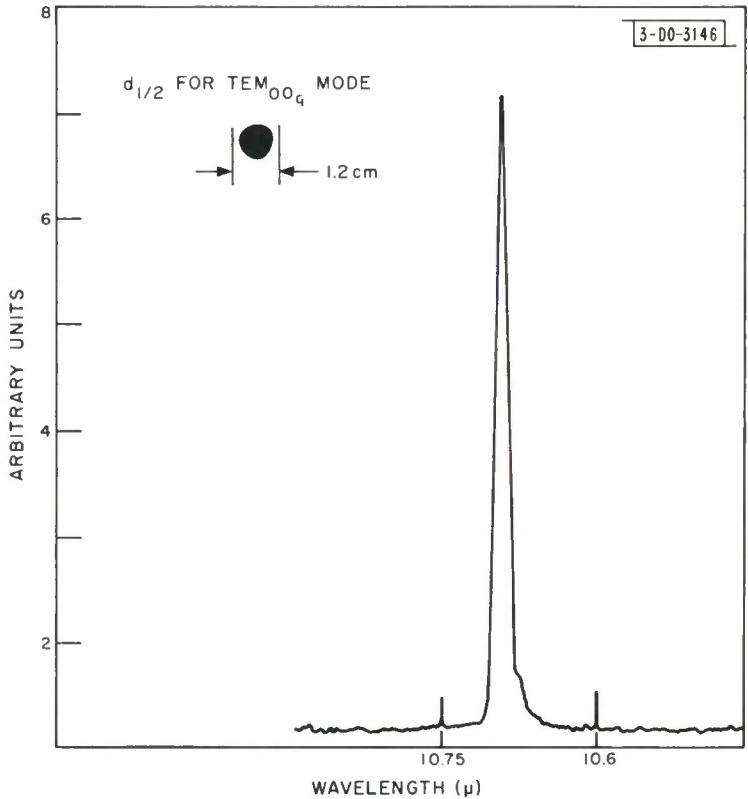


Fig. II-7. Spectrum of single mode CO₂ loser shown with spot size which was taken at distance from loser output.

REFERENCES

1. R. J. Glauber, "Photon Counting and Field Correlations," in Physics of Quantum Electronics Conference, Puerto Rico, June 1965, P. L. Kelley, B. Lax, and P. E. Tannenwald, editors (McGraw-Hill, New York, 1966), p. 788.
2. H. A. Haus, IEEE J. Quant. Electron. QE-1, 179 (1965).
3. C. S. Fuller, et al., Phys. Rev. 93, No. 6, 1182 (1954).
4. Solid State Research Report, Lincoln Laboratory, M. I. T. (1965:2), p. 20, DDC 624611.

III. MATERIALS RESEARCH

A. VAPOR GROWTH OF IODINE SINGLE CRYSTALS

Iodine single crystals used in solid state investigations are generally prepared by open-tube sublimation techniques¹ which yield a large number of relatively small platelets, rather than one large boule. The larger platelets may be up to 3 mm thick and have flat faces up to about 1 cm² in area. We have developed a simple method for growing large single crystals of iodine, exceeding 1 cm in their smallest dimension, by sublimation in a closed ampule. To establish the required vapor pressure and temperature gradient, the ampule is immersed in a water bath heated to ~75°C.

The ampules used in the present experiments are made from 15-mm i.d. pyrex tubing. Each has a flat bottom and is tapered to a point at the upper end, which is sealed to a pyrex support rod about 6 mm in diameter and 25 cm long. The ampule length is 9 cm and the volume is 25 cm³. In a typical experiment, an ampule is loaded with about 12 g of reagent grade polycrystalline iodine, evacuated with a mechanical fore pump, and sealed off. It is then suspended vertically, by means of the support rod, in a water bath contained in an 800-cm³ pyrex beaker with a loosely fitting glass cover. The tapered end of the ampule is initially placed just below the surface of the water, which is then heated to 70° to 75°C with an ordinary dial-adjusted hot plate. As the water level slowly falls because of evaporation through openings in the glass cover, the narrow tip is the first part of the ampule to emerge from the water and become cool enough for the iodine vapor to condense. Therefore, initial deposition is restricted to a very small area, and a single crystal is nucleated. After about 16 hours, the crystal, which exhibits two or three growth facets, has grown to a volume of about $\frac{1}{3}$ cm³. The hot plate is then turned off, and the water bath is allowed to cool slowly to room temperature.

For further crystal growth, the ampule is transferred to the pyrex "kettle" shown in Fig. III-1. This vessel has a glass cover with four openings, each sealed with a one-hole rubber stopper. The support rod of the ampule passes through the central stopper, and the ampule's height is adjusted so that its upper tip is initially at water level. One stopper is used to support a thermometer whose bulb is placed at about the midpoint of the ampule. The other two stoppers are used as vents to permit vapor to escape from the water bath, which is maintained at 70° to 75°C near the ampule by means of a hot plate.

After the ampule is transferred to the kettle, the iodine single crystal grows downward at about the same rate as the water level falls because of evaporation. Once it has grown a short distance below the tip of the ampule, the crystal itself does not remain in contact with the ampule wall; however, a thin dark layer of iodine condenses on the wall down to about the water level. If the temperature isotherms are parallel to the water level in the neighborhood of the growth interface, the bottom of this dark layer will be horizontal. If this is not the case, the temperature distribution in the bath is adjusted by placing thin asbestos sheet insulation at appropriate positions on the outside of the kettle.

Section III

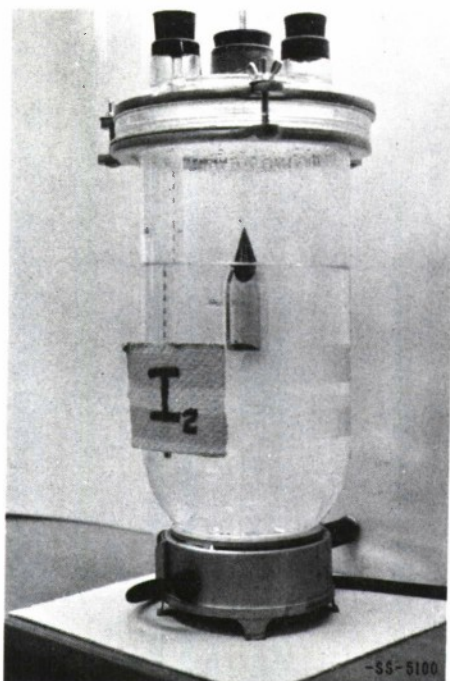


Fig. III-1. Apparatus for growth of iodine single crystals by sublimation in closed ampule. Crystal grown by this method is seen at upper end of ampule.

Fig. III-2. Close-up view of iodine single crystal shown in Fig. III-1.



A single crystal grown in the manner described is shown inside the ampule in Fig. III-1. Figure III-2 is a close-up view of this crystal, which has two large, highly reflecting facets at the growth interface. The crystal is cone shaped, reaching a maximum diameter of about 1.6 cm, and then rounding off near the bottom. The total length is about 4 cm. This crystal was grown in a period of two weeks, but significantly faster growth rates seem feasible.

S. Fischler

B. PARTIAL PRESSURES OF $\text{Te}_2(\text{g})$ IN EQUILIBRIUM WITH $\text{Ge}_{1/2-\delta}\text{Te}_{1/2+\delta}(\text{c})$

The partial pressures of $\text{Te}_2(\text{g})$ in equilibrium with Ge-Te samples containing 1.00, 49.84, 49.92, 50.00, 50.08, 50.30, 50.60, 50.70, 50.85, 51.01, 51.5, and 52.0 atomic-percent Te have been determined by measuring the optical density of the vapor at 4357 and 5000 Å. The general technique has been described previously.² The samples were prepared by heating weighed quantities of the semiconductor grade elements totaling 15 g to 950°C, quenching, breaking the resulting ingot into pieces in the 0.1- to 1.0-mm range, and finally annealing for ten days at about 550°C. All heating was carried out in sealed, evacuated silica tubes that had been previously outgassed for sixteen hours at 1020°C and 10^{-6} torr.

The results for the various Ge-Te compositions are shown in Fig. III-3, where the optical density at 4357 Å for a 101.3-mm optical path at 1000°C is plotted on a logarithmic scale against the reciprocal absolute temperature of the condensed phases providing the vapor. The partial pressure of $\text{Te}_2(\text{g})$ is related to D_{4357} by

$$p_{\text{Te}_2}(\text{atm}) = (3.12 \times 10^{-3}) D_{4357}$$

Figure III-4 shows a temperature-composition projection of the Ge-Te phase diagram in the vicinity of the equiatomic composition, which has been constructed on the basis of the data shown in Fig. III-3. The dashed portion of the Ge-rich solidus is drawn to be consistent with published results³ near 450°C. It is seen that the width of the homogeneity range is about 1.3 atomic-percent, similar to that for SnTe ⁴; but, in contrast to SnTe , the homogeneity range includes compositions of less than 50 atomic-percent Te at temperatures above 600°C (the lowest temperature measured). The maximum melting point of $\text{Ge}_{1/2-\delta}\text{Te}_{1/2+\delta}(\text{c})$ is shown at a composition of less than 50 atomic-percent Te. This result follows from the fact that near 710°C, D_{4357} for the 50.00 atomic-percent sample decreases with increasing temperature, since this shows that 50.00 atomic-percent must lie on the Te-rich three-phase line in this temperature range. McHugh and Tiller⁵ have reported that the maximum melting composition is 50.6 atomic-percent Te.

Values for the Gibbs free energy of $\text{GeTe}(\text{c})$ and for the partial molal enthalpy and entropy of Te in $\text{Ge}_{1/2-\delta}\text{Te}_{1/2+\delta}(\text{c})$ have been obtained by thermodynamic analysis of the data shown in Fig. III-3 (see Ref. 6).

R. F. Brebrick

Section III

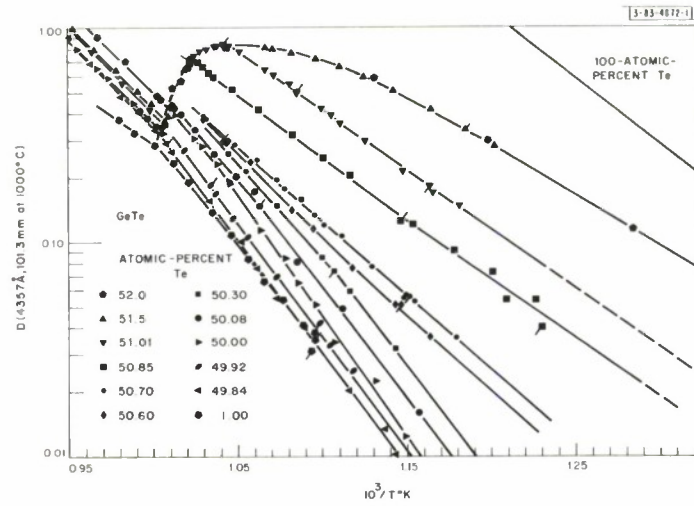


Fig. III-3. Optical density at 4357 Å on a logarithmic scale plotted against reciprocal absolute temperature for various values of atomic-percent Te in the Ge-Te system. A line slanting up and to the right from a point indicates sample was at temperature for 16 hours before measurement. A line slanting down and to the left from a point indicates that measurement was taken within about 1 hour after sample was at 680°C.

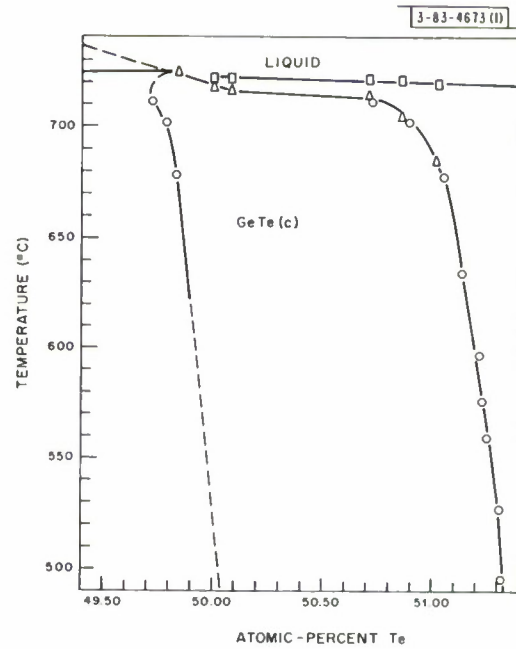


Fig. III-4. Temperature-composition projection of Ge-Te phase diagram in vicinity of equiatomic composition, constructed on basis of data shown in Fig. III-3.

C. NEW PHASE TRANSFORMATION IN InSb AT HIGH PRESSURES AND TEMPERATURES

The high-pressure phase of InSb with β -Sn structure, InSb(II), can be retained at atmospheric pressure by cooling to below 180°K before removing the pressure. This phase has a superconducting transition temperature of 2.1°K. In recent solution calorimetry experiments* at atmospheric pressure, undertaken to measure the heat of transformation of InSb(II) to the atmospheric pressure form InSb(I), it was found that the quantity of heat evolved on solution in molten tin was significantly different for samples annealed close to liquidus temperature than for those annealed at lower temperatures. Furthermore, the higher temperature samples had x-ray diffraction patterns at 170°K and atmospheric pressure inconsistent with the β -Sn structure, and their superconducting transition temperature T_c was 4.0° to 4.1°K. These observations suggested the possibility of a new high-pressure phase transformation in InSb at elevated temperatures. The existence of such a transformation, to a phase which we have designated as InSb(III), has been confirmed by measurements of T_c as a function of annealing temperature.

The samples to be measured were annealed in a belt-type high-pressure unit. Some were held at 450°C, above the liquidus, for an hour prior to annealing at lower temperature, while the rest were not melted before annealing. After annealing, the belt unit was cooled to about 130°K before the pressure was released, in order to retain the high-pressure phase. One series of samples was prepared at 37 kbar by annealing for 20 hours, a period found to be long enough to establish equilibrium at all the temperatures investigated. The T_c values, which were measured by a self-inductance technique, are plotted against annealing temperature in Fig. III-5. The abrupt change in T_c between 300° and 315°C shows that at 37 kbar the transformation from InSb(II) to InSb(III) occurs at $308^\circ \pm 7^\circ\text{C}$.

A second series of samples was annealed at 52 kbar. To establish equilibrium at this pressure, it was necessary to anneal for 40 to 100 hours, depending on temperature. Until equilibrium was reached, the samples exhibited two superconducting transitions. The plot obtained for T_c vs annealing temperature establishes the transformation temperature at $387^\circ \pm 12^\circ\text{C}$ for 52 kbar. Therefore, the slope dT/dp is negative for the phase boundary between InSb(II) and InSb(III).

Kasper and Brandhorst⁷ have reported that a phase with orthorhombic structure is the stable phase of InSb above 30 kbar at room temperature. Additional data supporting this conclusion have been obtained by McWhan and Marezio.⁸ On the basis of the data so far available, it is not possible to decide whether or not InSb(III) and the orthorhombic phase are the same. There is some evidence, however, that the two phases are different. Thus, it appears that InSb(III) would be stable at room temperature only at pressures appreciably greater than 52 kbar, rather than at about 30 kbar. In addition, preliminary x-ray data for InSb(III) are inconsistent with the orthorhombic structure, and the scattered T_c values for the orthorhombic phase reported by McWhan and Marezio⁸ are generally lower than the value of 4.1°K observed for InSb(III).

The existence of InSb(III) apparently explains a discrepancy in T_c data reported earlier for the high-pressure InSb-Sn system. According to our measurements,⁹ T_c abruptly increases

* These experiments are being performed by Dr. A. K. Jena and Professor M. B. Bever, Department of Metallurgy, M.I.T.

Section III

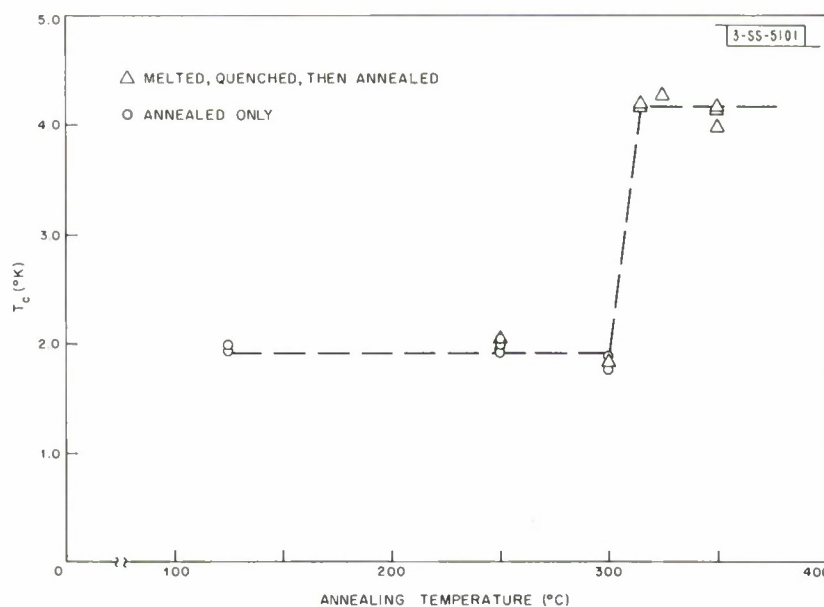


Fig. III-5. Superconducting transition temperature T_c of InSb plotted against temperature of annealing at 37 kbar.

from 2.1° to about 4°K on the addition of only a few atomic-percent Sn, then rises to a maximum of about 5°K, and finally decreases to the value of 3.8°K observed for β -Sn. Tittman, *et al.*,¹⁰ however, reported a gradual monotonic increase in T_c from 2.1° to 3.8°K with increasing Sn content. Since our samples containing Sn were prepared at 37 kbar by annealing well above 315°C, they are presumably solid solutions with the InSb(III) structure, while Tittman's samples probably have the InSb(II) structure.

M. D. Banus
M. C. Lavine

D. PSEUDO-BINARY InSb-InTe SYSTEM AT 37 kbar

Earlier studies¹¹ of the pseudo-binary InSb-InTe system at 37 kbar have been continued by making additional x-ray diffraction and superconductivity measurements on samples covering the composition range between 60 and 100 mole-percent InTe. Specimens for high-pressure annealing were prepared from mixtures of high-purity InSb and InTe powders. These mixtures were melted in evacuated quartz ampules for 2 hours at about 750°C, quenched in cold water, crushed to ~100 mesh, blended, and pressed into cylinders. One portion of each sample was analyzed chemically for In, Sb, and Te. The cylinders were either used without further treatment or were first annealed in evacuated quartz ampules for 3 to 4 weeks at 480°C. Both types of cylinders were annealed at 37 kbar, in either a belt-type or a tetrahedral-anvil pressure unit, for 20 hours at 500° ± 10°C. The samples were cooled to room temperature before the pressure was released, in order to retain the high-pressure phases. They were stored at dry-ice temperature to prevent the slow transformation of high-pressure InTe(II), if present, into the stable phase at atmospheric

pressure, InTe(I). The lattice constants a_0 of the samples, all of which had the rocksalt structure, were determined from Debye-Scherrer patterns by means of a least-squares extrapolation. The superconducting transition temperatures T_c were measured by a self-inductance technique.

The measured values of a_0 and T_c are plotted against sample composition in Figs. III-6 and III-7, respectively. Both parameters generally increase with increasing InTe content. (Superconducting transitions were not observed for compositions below 74 mole-percent InTe, since our apparatus cannot detect transitions below 1.3°K.) The data indicate that there are single-phase regions which extend from 60 to at least 80 mole-percent InTe, and from pure InTe down to at least 90 mole-percent InTe. However, there is sufficient scatter in the data between 80 and 90 mole-percent InTe to suggest that a two-phase region may be located in this composition range. Furthermore, several samples within this range exhibited broad superconducting transitions similar to those observed for finely dispersed two-phase specimens. However, no sample gave two distinct superconducting transitions, and no sample could be identified as two-phase on the basis of its x-ray diffraction pattern. Therefore, on the basis of the data so far available, it cannot be decided whether there is complete solid solubility at 37 kbar from 60 to 100 mole-percent InTe, or whether there is a miscibility gap in the region between 80 and 90 mole-percent InTe.

At 84 mole-percent InTe, samples annealed in the tetrahedral-anvil press have significantly higher values of T_c than those annealed in the belt unit. At 87 mole-percent InTe, samples prepared from "as-melted" cylinders have higher values of both T_c and a_0 than those prepared from cylinders pre-annealed at 480°C. No explanation has been found for either of these observations.

It was previously reported¹¹ that InSb-InTe samples containing 75 mole-percent InTe exhibited a superconducting transition if they were annealed at high pressure, but not if they were prepared at atmospheric pressure or if they were re-annealed at atmospheric pressure after high-pressure treatment. These observations can easily be explained on the basis of the present high-pressure results, together with the phase diagram for the InSb-InTe system at atmospheric pressure.¹² At atmospheric pressure, the samples are two-phase mixtures of InTe(I), which is not a superconductor, and In_3SbTe_2 , which has a superconducting transition at 1.06°K (Ref. 13), too low in temperature to be detected by our apparatus. At 37 kbar, however, the samples consist of a single phase containing 75 mole-percent InTe, whose superconducting transition can be detected by our apparatus.

M. D. Banus
Mary C. Finn
M. Jane Button

E. EXPERIMENTAL ATOMIC FORM FACTORS IN MgO

X-ray diffraction data for MgO have recently been reported by Burley¹⁴ and Togawa.¹⁵ Burley found that his experimental results were consistent with the theoretical atomic form factors for oxygen in MgO given by Suzuki,¹⁶ while Togawa concluded that his data were consistent with the theoretical form factors of Tokonami.¹⁷ In order to resolve this disagreement, an x-ray diffraction study has been made on high-purity MgO powder. The relative intensities of ten diffraction lines were measured at room temperature with a General Electric XRD-5

Section III

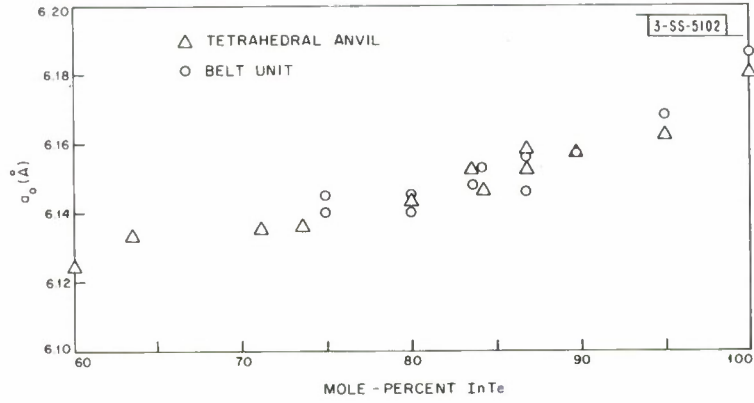


Fig. III-6. Lattice parameter a_0 plotted against composition for InSb-InTe samples annealed at 37 kbar and 500°C.

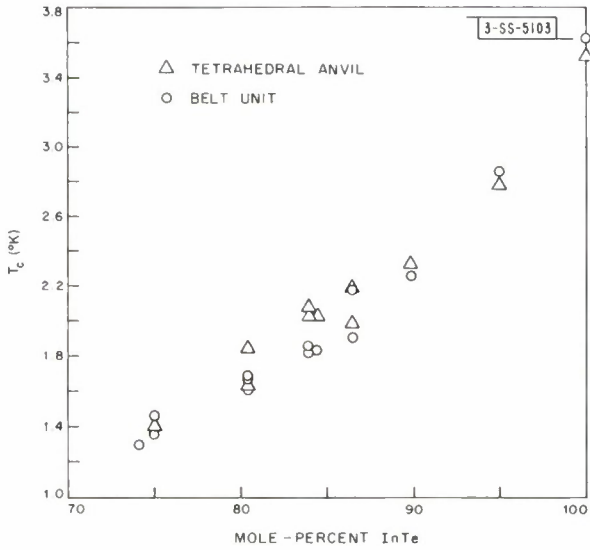


Fig. III-7. Superconducting transition temperature T_c plotted against composition for InSb-InTe samples annealed at 37 kbar and 500°C.

diffractometer using nickel-filtered $\text{Cu K}\alpha$ radiation. For each line, the integrated intensity was obtained by measuring the total count while the peak was scanned several times and by subtracting the appropriate background correction. Measurements on three different samples gave intensities reproducible to about 0.4 percent of the total observed intensity.

In order to test the agreement between theory and experiment, the scaling factor and the Debye-Waller factors for magnesium and oxygen were considered as parameters, and their values were adjusted by a computer program to minimize the function

$$R = \frac{\sum_{\text{hkl}} |I_{\text{obs}}(\text{hkl}) - I_{\text{calc}}(\text{hkl})|}{\sum_{\text{hkl}} I_{\text{obs}}(\text{hkl})}$$

where $I_{\text{obs}}(\text{hkl})$ and $I_{\text{calc}}(\text{hkl})$ are, respectively, the observed and calculated relative intensities of the line with Miller indices (hkl) . Two separate calculations were made, one using values of I_{calc} obtained from the oxygen form factors of Suzuki, and the other based on the form factors of Tokonami. The same scattering function for magnesium¹⁸ was used in both calculations.

The minimum values of R calculated by using the oxygen form factors of Suzuki and Tokonami are 0.849 and 0.681, respectively. Both values are comparable with the experimental reproducibility of about 0.4 percent, and the difference between them is not sufficient to permit a choice between the two theoretical treatments. However, comparison of the observed and calculated structure factors for the individual diffraction lines reveals a significant difference between the two calculations. For the Suzuki calculation, the discrepancies between the observed and calculated structure factors are systematically greater for the lines with (hkl) all odd than for those with (hkl) all even. No such distinction between the two sets of lines is apparent for the Tokonami calculation. We therefore conclude, in agreement with Togawa, that the experimental data are more consistent with the form factors of Tokonami than with those of Suzuki.

Since the analysis just described requires the use of theoretical values for the atomic form factors, it does not permit the determination of the form factors directly from the experimental data. In order to make such a determination, relative intensity measurements on the MgO powder samples were made at nine additional temperatures between room temperature and 500°C , giving a total of 100 observed intensities. A computer program was then used to minimize the factor R by optimizing the values of 41 adjustable parameters: the scaling factor, one temperature factor for oxygen and one for magnesium at each temperature, and one form factor for magnesium and one for oxygen for each line. The form factors were taken to be independent of temperature on the assumption that the charge distribution in MgO does not depend on temperature over a range sufficiently remote from the melting point (2800°C). The change in line position due to thermal expansion was taken into account by using the equation $a_{\text{O}}(\text{\AA}) = 4.21 + (5.44 \times 10^{-5}) t^\circ\text{C}$, which was obtained by least-squares analysis of the data.

The atomic form factors obtained by the method described are listed in Table III-1, together with the theoretical form factors of Tokonami and Suzuki for oxygen and the published form factors for magnesium.¹⁸ Consistent with the conclusion reached on the basis of room-temperature data, the experimental results for oxygen are in better agreement with the values of Tokonami than with those of Suzuki. However, the discrepancy between experimental and theoretical factors

TABLE III-1 ATOMIC FORM FACTORS IN MgO					
(hkl)	Oxygen			Magnesium	
	Experimental	Theoretical			
		Takanami*	Suzuki†	Experimental	Theoretical‡
111	5.86	6.05	5.78	8.62	8.68
200	5.36	5.36	5.12	8.43	8.31
220	3.79	3.69	3.53	7.16	7.03
311	3.02	3.04	2.97	6.23	6.29
222	2.88	2.87	2.83	6.05	6.07
400	2.58	2.41	2.43	5.06	5.29
331	2.36	2.19	2.24	4.92	4.84
420	2.15	2.13	2.18	4.62	4.69
422	1.99	1.95	2.00	4.10	4.21
333	1.83	1.85	1.89	3.70	3.90

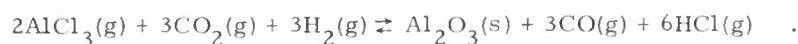
*Ref. 17.
†Ref. 16.
‡Ref. 18.

for the [111] line indicates that some additional improvement in the theory should be attempted.

P. M. Raccach
R. J. Arnott

F. LASER PROPERTIES OF VAPOR-GROWN RUBY

Crystals of α -alumina have been grown from the vapor phase¹⁹ by the following reaction



The same reaction has now been used to grow ruby crystals* by substituting a small fraction of $\text{CrCl}_3(\text{g})$ for $\text{AlCl}_3(\text{g})$. Both of these chlorides are produced by passing Cl_2 (99.5%) over heated Al or Cr metals. These gases, as well as H_2 (99.8%) and CO_2 (99.5%), are purged of O_2 and H_2O and then vacuum pumped at controlled rates past a heated Al_2O_3 substrate supported within an alumina reactor tube.

The laser properties of a vapor-grown ruby rod (0.01% Cr_2O_3) were compared with those of commercial Verneuil pink (0.005% Cr_2O_3) and Czochralski red (0.05% Cr_2O_3) rods. The Cr_2O_3 concentration of the vapor-grown ruby was determined by three different methods. Specimens for analysis were obtained from the same general area of the crystal and all had the same dopant

* Vapor-grown ruby was kindly supplied by P. S. Schaffer of Lexington Laboratories, Inc., Cambridge, Mass.

concentration, as nearly as could be detected visually. All rods were fabricated to the same specifications and the end faces silvered for either 0- or 1-percent transmission. The rods were held by a cold finger cooled to 77°K, and were pumped by two FX-51 flashlamps. The temperature of the laser crystal was approximately 90°K. Threshold energies for laser oscillation were measured as follows: vapor-grown ruby – 25J; Czochralski ruby – 28J; and Verneuil ruby – 41J. Laser threshold depends on several parameters and varies markedly with crystal quality as well as Cr^{+3} concentration.²⁰ Because of the low Cr concentration, the pink ruby was expected to have a high threshold. For the same reason, the vapor-grown crystal should have a threshold 30 percent higher than the Czochralski crystal. The fact that the thresholds were approximately the same indicates that the crystal quality of the vapor-grown material is quite high. However, the results should be construed as qualitative until additional crystals are investigated.

Figures III-8(a-c) show laser emission from the vapor-grown ruby. In each picture, the upper trace shows the lamp output and the lower trace shows fluorescence and laser output of the rod monitored by a photomultiplier tube through interference filters. Figure III-8(a) is just below threshold; Fig. III-8(b) is just above threshold at a lamp input of 25J; and Fig. III-8(c) is 40 percent above threshold and clearly shows that the output from the rod has a large CW component. The reason for this quasi-CW operation is not clearly understood. Both the pink and red ruby rods showed the usual spiking associated with relaxation oscillations.²¹

J. R. O'Connor

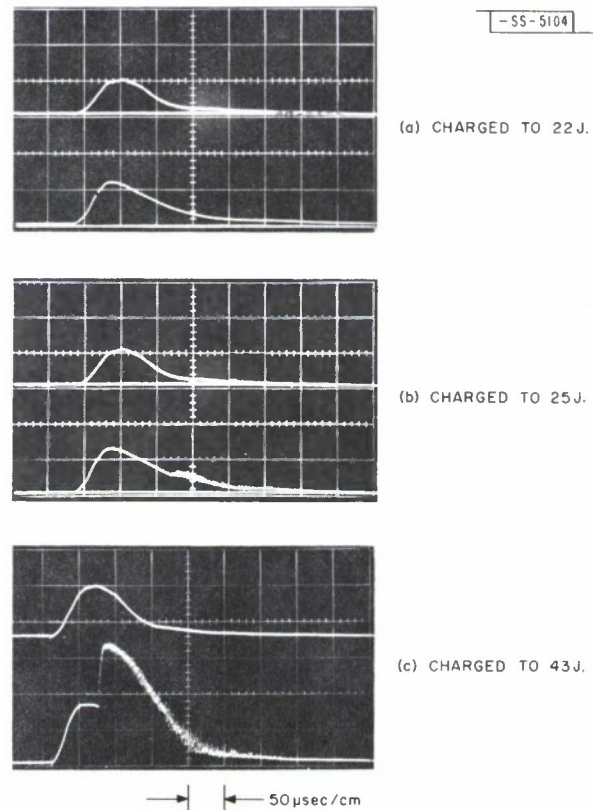


Fig. III-8(a-c). Flashlamp intensity and laser emission from vapor-grown ruby as function of time. In each picture, upper trace shows output of flashlamp; lower trace shows both fluorescence and laser emission from ruby. Laser cavity was cooled to 90°K.

G. CHEMICAL ANALYSIS

1. Complexometric Titrations

Continued use of the method reported previously²² for analyzing rare earth cobalt oxides revealed that the potentiometric titration employed to determine the rare earth element was subject to appreciable errors. These errors occurred because the gold-amalgam electrode used in the titration was occasionally attacked by the KCN added to complex the cobalt. In order to eliminate this source of error, a different procedure has been adopted for the rare earth determination. In the new method, the cobalt is masked with KCN, the rare earth is complexed with EDTA, and formaldehyde is added dropwise to remove the excess KCN. The excess EDTA is then titrated at pH 10 with MgSO_4 solution to a colorimetric end point, using a freshly made Eriochrome Black T solution as indicator. The method is accurate to about three parts per thousand.

As in the original procedure, the total of rare earth plus cobalt is determined on a separate aliquot by complexing with EDTA and titrating the excess EDTA with copper solution to a potentiometric end point at a pH between 8.3 and 8.6.

E. B. Owens
Maria A. Rabbio
J. C. Cornwell

2. X-Ray Fluorescence Analysis

a. Lanthanum Cobalt Oxide

An x-ray fluorescence method has been developed for determining the major constituents in lanthanum cobalt oxide. A 100-mg sample is dissolved in 8-ml HNO_3 and diluted to 100 ml. Appropriate standards are made from stock solutions of pure cobalt metal and lanthanum oxide. The concentrations of the stock solutions are checked by EDTA titrations.

The fluorescence spectra of the standard and sample solutions are excited by the radiation from a tungsten x-ray tube operated at 45 kV and 35 mA. The K_α line of Co is measured with a scintillation counter, LiF analyzing crystal, and air path. The K_α line of La is measured with a gas flow counter (P10 gas), EDDT analyzing crystal, and H_2 path. A pulse-height analyzer is used for both elements. No absorption or enhancement corrections are made.

This method gives the same results as the EDTA titration method described in the preceding section and is much faster.

b. Iron-Nickel-Copper Thin Films

An x-ray fluorescence method has been developed for the analysis of iron-nickel-copper films 100 to 300 Å thick, which are deposited on glass substrates. A special fixture of pure silver was made to hold the film on its substrate in the radiation from a tungsten tube operated at 45 kV and 35 mA. The K_α lines of the three principal elements are measured using a scintillation counter, an LiF analyzing crystal, an air path, and a pulse-height analyzer. The method is calibrated with films analyzed by the spectrophotometric method reported previously.²³ No absorption or enhancement corrections are made.

Within the experimental error of several parts per thousand, the fluorescence method gives the same results as the spectrophotometric method and requires only about one-tenth the time.

E. B. Owens
Maria A. Rabbio

3. Electron Microprobe Analysis

A method has been developed for determining Se and S in $\text{CdSe}_x\text{S}_{1-x}$ alloys by electron microprobe analysis. The samples which have been analyzed are thin vapor-grown platelets used in laser experiments.²⁴ Separate x-ray spectrometers are used to make simultaneous intensity measurements of the third order $K_{\alpha 1}$ line of Se ($\lambda = 1.105 \text{ \AA}$) and of the first order $K_{\alpha 1}$ line of S ($\lambda = 5.372 \text{ \AA}$). Several areas of each sample are examined. Intensity measurements of the Se and S lines are also made on platelets of pure CdSe and CdS, respectively, which are used as standards.

The quantity of alloy material available was not large enough to permit experimental calibration of the microprobe analysis. Therefore, calibration curves for Se and S in the $\text{CdSe}_x\text{S}_{1-x}$ system were calculated by using the backscattered electron correction of Duncumb and Shields,²⁵ the ionization correction of Nelms,²⁶ and the absorption correction of Philibert.²⁷ The Se curve is used to obtain the mole-fraction of CdSe present in each sample from the ratio of the Se line intensity measured for the sample to the intensity of this line measured for pure CdSe. Similarly, the S curve is used to obtain the mole-fraction of CdS from the intensities of the S line measured for the sample and for CdS.

The mole-fractions of CdSe found for five alloy samples are given in Table III-2. The first column lists the value obtained directly from the Se measurements. The second column gives

From Se Determination	From S Determination (by difference)	Average
0.10	0.14	0.12
0.37	0.40	0.39
0.53	0.53	0.53
0.76	0.77	0.77
0.79	0.79	0.79

the value found by difference from the mole-fraction of CdS obtained from the S data. The two sets of values, which are based on independent measurements, are in good agreement, particularly for those samples containing more than 0.5 mole-fraction CdSe.

Mary C. Finn

REFERENCES

1. A.A. Brener and R. Chen, *J. Phys. Chem. Solids* 24, 135 (1963); M. Simhony, *J. Phys. Chem. Solids* 24, 1297 (1963).
2. R. F. Brebrick, *J. Chem. Phys.* 41, 1140 (1964); R. F. Brebrick and A.J. Strauss, *J. Phys. Chem. Solids* 26, 989 (1965).
3. L.Ye. Shelimova, N.Kh. Abrikosov, and V.V. Zhdanova, *Zh. Neorgan. Khim.* 70, 1200 (1965).
4. R. F. Brebrick and A.J. Strauss, *J. Chem. Phys.* 41, 197 (1964).
5. J.P. McHugh and W.A. Tiller, *Trans. Met. Soc. AIME* 218, 187 (1960).
6. R. F. Brebrick, *J. Phys. Chem. Solids* (to be published).
7. J.S. Kasper and H. Brandhorst, *J. Chem. Phys.* 41, 3768 (1964).
8. D.B. McWhan and M. Marezio, private communication.
9. S.D. Nye, M.D. Banus, and H.C. Gatos, *J. Appl. Phys.* 35, 1361 (1964); M.D. Banus, S.N. Vernon, and H.C. Gatos, *J. Appl. Phys.* 36, 864 (1965), DDC 616443.
10. B.R. Tittman, A.J. Darnell, H.E. Bommel, and W.F. Libby, *Phys. Rev.* 135, A1460 (1964).
11. Solid State Research Reports, Lincoln Laboratory, M.I.T. (1964:1), p.34, DDC 601830, H-587; (1964:3), p.35, DDC 609828, H-627.
12. K. Deneke and A. Rabenau, *Z. Anorg. Allgem. Chem.* 333, 201 (1964); A.J. Strauss, M.D. Banus, and M.C. Finn, *J. Electrochem. Soc.* 113, 458 (1966).
13. A. Rabenau, K. Deneke, and M.M. van der Meij, *Angew. Chem.* 76, 651 (1964).
14. G. Burley, *J. Phys. Chem. Solids* 26, 1605 (1965).
15. S. Togawa, *J. Phys. Soc. Japan* 20, 742 (1965).
16. T. Suzuki, *Acta Cryst.* 13, 279 (1960).
17. M. Tokonami, *Acta Cryst.* 19, 486 (1965).
18. International Tables for X-ray Crystallography (The Kynoch Press, Birmingham, 1962), Vol. III., p.202.
19. P.S. Schaffer, *J. Am. Ceram. Soc.* 48, 508 (1965).
20. I.J. D-Haenens and V. Evtuhov, Quantum Electronics III (Columbia University Press, New York, 1964), p.1134.
21. H. Statz and G. De Mars, Quantum Electronics (Columbia University Press, New York, 1960), p.530.
22. Solid State Research Report, Lincoln Laboratory, M.I.T. (1965:3), p.33, DDC 629048.
23. ibid., p.34.
24. C.E. Hurwitz, *Appl. Phys. Letters* 8, 243 (1966).
25. P. Duncumb and P.K. Shields, Proceedings of the Electron Probe Symposium, Washington, D.C., 1964 (to be published).
26. A.T. Nelms, *Natl. Bur. Std. Cir.* 577 (1956) and Supplement (1958).
27. J. Philibert, Proceedings of the Third International Symposium on X-ray Optics and X-ray Microanalysis (Academic Press, New York, 1964), p.379.

IV. PHYSICS OF SOLIDS

A. ELECTRONIC BAND STRUCTURE

1. Optical Constants of ReO_3

Since the last Solid State Research Report,^{*} the reflectivity measurements on ReO_3 have been extended from 12 to 22 eV. The significant features found in this new range are a peak of 15 percent near 14 eV, then a slowly dropping reflectivity reaching about 9 percent at 22 eV. The analysis described in the last report has been extended to include the new data. The results for the region below 12 eV have not been significantly altered by the new measurements.

The complete interpretation of the optical data, particularly the high-energy interband structure, must await an accurate band calculation. We have attempted to adapt a tight binding calculation for SrTiO_3 (Ref. 1) to examine some of the low-energy structure in ReO_3 by using the Fourier expansion technique of Dresselhaus² and including the appropriate spin-orbit interaction. The method was applied to the t_{2g} conduction bands, and assumes that the oxygen and e_g bands are well separated from the lowest lying split-off conduction band. For various values of the two adjustable Fourier coefficients, the Fermi level was determined by a Monte Carlo sampling procedure. An examination of the resulting Fermi surface in relation to the higher bands enabled us to determine the low-energy transitions to higher conduction bands.

The initial results indicate that, with a spin-orbit parameter of 1.2 eV, very weak transitions would be expected to occur before the plasma edge at 2.2 eV. However, although no such structure is found in the reflectivity data, such transitions could result in an apparent short scattering time.

J. Feinleib
W. J. Scouler

2. Exciton Structure and Zeeman Effects in GaSe at 1.5°K [†]

Using relatively unstrained samples which were previously not available, we have been studying the magnetoabsorption spectrum of GaSe in the excitonic rather than in the Landau region; complete linear and diamagnetic spectra of the former give both the electron and hole masses and g-factors. The present experiments use the Faraday geometry, circularly polarized radiation, and spectrographic techniques which give resolving powers of the order of 70,000.

We have observed the linear Zeeman splitting and diamagnetic shift of the 1S level. This is shown in the curves at the bottom of Figs. IV-1 and IV-2. As a first approximation, we use the analysis of Wheeler and Dimmock³ for CdSe , although GaSe may be somewhat more anisotropic than CdSe and hence not as readily amenable to a perturbation calculation in terms of hydrogenic-like functions. From the linear splitting of the 1S level, we then determine $g_{\text{hz}} - g_{\text{ez}} = -2.6$. It

* Solid State Research Report, Lincoln Laboratory, M.I.T. (1966:1), p. 33, DDC 632998, II-721.

† This experiment was carried out using the high field facilities of the National Magnet Laboratory, M.I.T.

Section IV

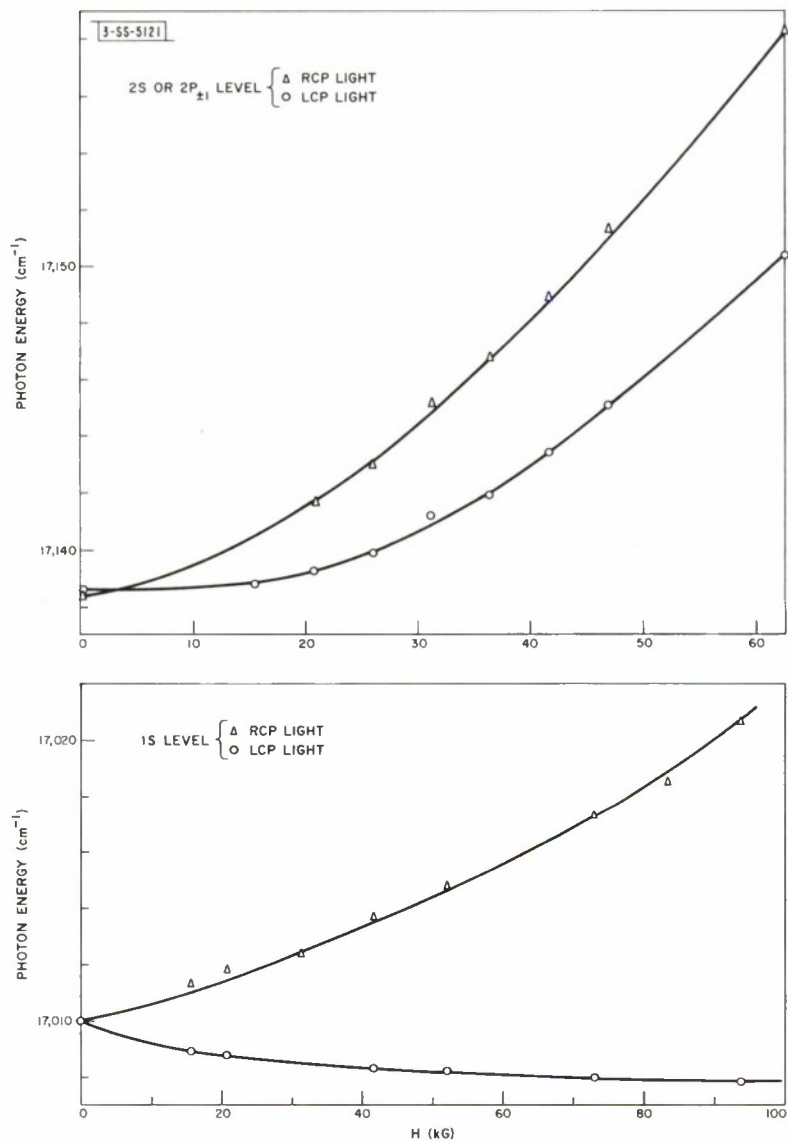


Fig. IV-1. Energies of observed exciton states as function of magnetic field for Faraday geometry and $H \parallel c$ -axis. Temperature is 1.5°K.

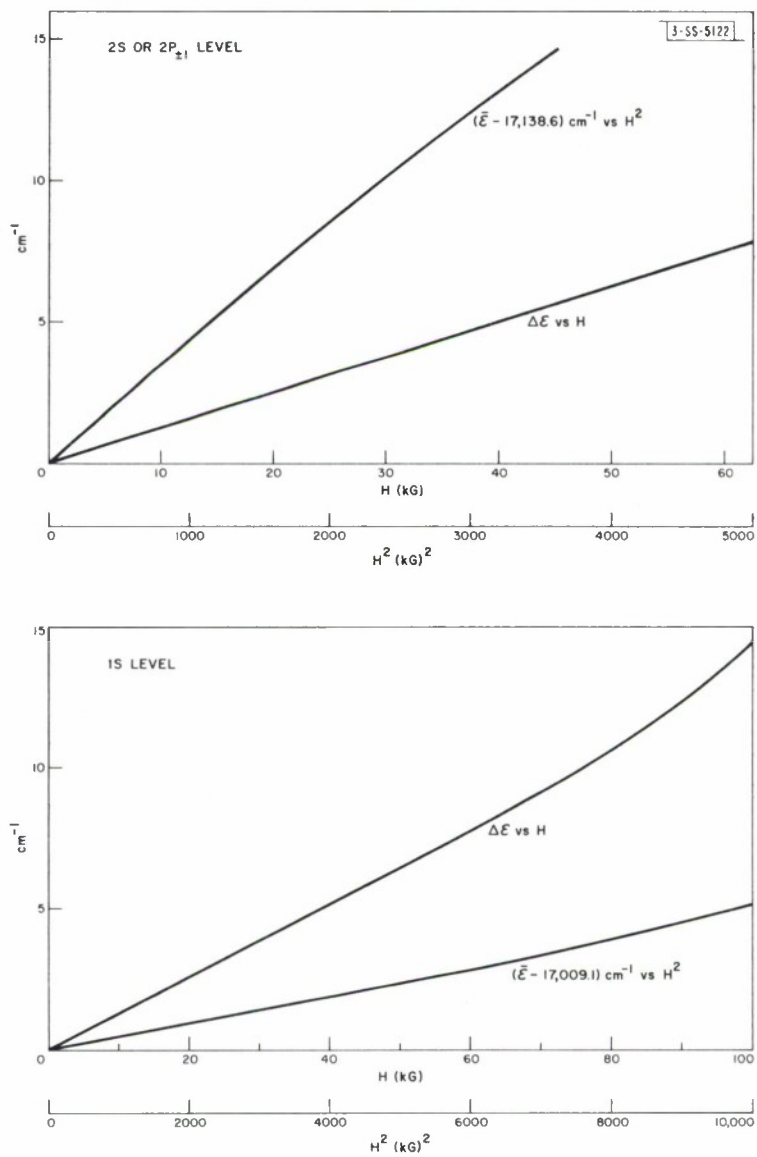


Fig. IV-2. Linear Zeeman splittings and diamagnetic shifts of observed exciton states.

Section IV

is difficult to extract any information out of the diamagnetic shift of this level because of the central cell correction; the 1S level is sufficiently tightly bound that the usual dielectric constant cannot be used.

We have also observed a second set of lines corresponding to either the $2P_{\pm 1}$ level or the 2S level. Their energies as a function of magnetic field and their linear and diamagnetic shifts are plotted at the top of Figs. IV-1 and IV-2, respectively. The identification is not at present unique, since both of these states couple to circularly polarized radiation and they have approximately the same diamagnetic shift.

J. Halpern

3. Polaron Induced Anomalies in InSb

Theoretical considerations have led us to anticipate large polaron effects in the interband magnetoabsorption in InSb. Recently, we have performed the appropriate experiments and have found the striking anomalies that were predicted. These results constitute the first direct and unambiguous observations of polaron self-energy effects, and they are consistent with previously published values of the band parameters and the longitudinal optical phonon energy. Most of the present conclusions concern one optical transition that we have examined in detail, although we have preliminary data showing polaron effects in other transitions. We have written a paper describing these experiments which has been published in the Physical Review Letters.⁴

E. J. Johnson
D. M. Larsen

4. Observation of Polaron Resonance in Intraband Magnetoabsorption in InSb

The observation of polaron anomalies in the interband magnetoabsorption of InSb (Sec. IV-A-3) has stimulated a search for similar effects near the optical phonon frequency in the intraband magnetoabsorption. Theory and the experimental interband results strongly suggest that the cyclotron resonance frequency should saturate with magnetic field as the field exceeds a critical value H_c . Here, H_c is defined as the field at which, in the absence of electron-longitudinal optical phonon interaction, the energy separation between the two adjacent spin-up conduction band Landau levels would equal $\hbar\omega$, the energy of a longitudinal optical phonon. The observed resonance frequency should approach ω asymptotically with increasing magnetic field.

The intraband effects are difficult to observe because of the intense background absorption in the region of saturation. The intraband results can be expected to corroborate the interband results and can be used in conjunction with them to account for effects due to excitons and to complications of the valence band.

Observations on an InSb sample at about 30°K show two slightly separated absorption lines, whose energies are approximately equal to the expected separation of the $n = 1$ and 0 spin-up Landau levels. Similar lines had been reported previously by Boyle and Brailsford.⁵ Just below the optical phonon frequency, the energy of each of the two lines begins to saturate with increasing magnetic field in qualitative agreement with the interband results. The observation of two lines, however, indicates that the situation is complicated and that further analysis is needed.

D. H. Dickey
E. J. Johnson
D. M. Larsen

5. Magneto-Piezo-Optical Studies in Semiconductors*

The piezo-optical technique has proven to be a very useful tool in providing information on the electronic band structure of solids.^{6,7} This method has been used to increase the spectral sensitivity in reflection and absorption experiments in semiconductors and metals.

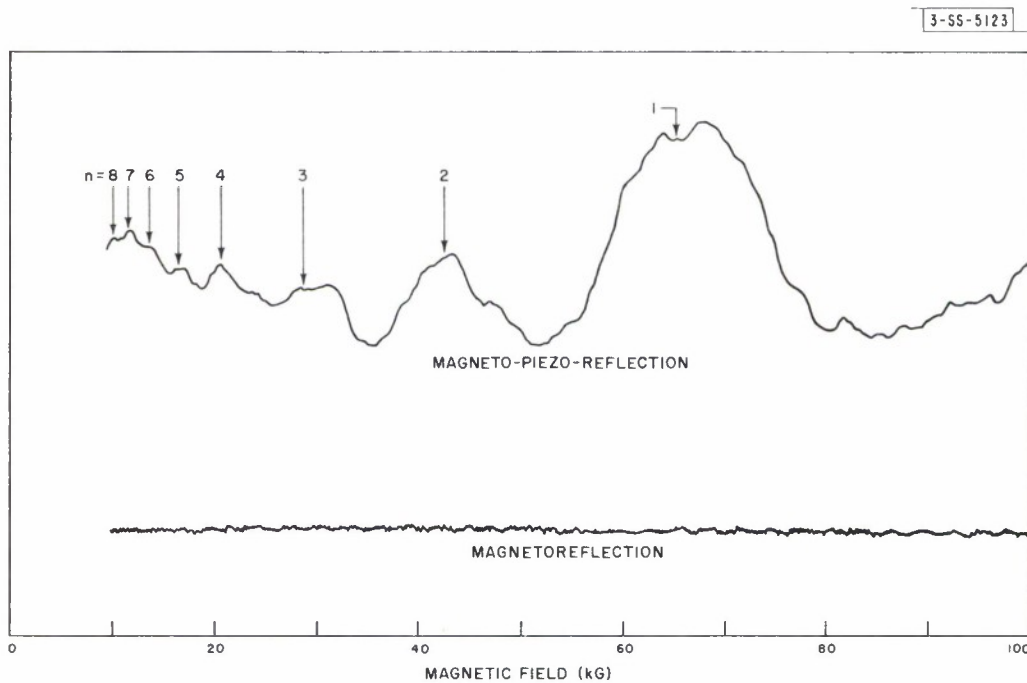


Fig. IV-3. Variation with magnetic field of reflectivity and piezo-reflectivity in Ge for $\hbar\omega = 0.826$ eV, just above direct energy gap. Temperature is 300°K.

It is well known that more-detailed information on the band structure can be obtained by performing optical experiments in a magnetic field. The application of a magnetic field to the differential piezo-optical technique also results in a marked improvement in the sensitivity of the magneto-optical measurements. The power of this technique has been demonstrated in the preliminary results that we have obtained in the magneto-piezo-reflectance experiments on the semiconductors, Ge and InSb. A comparison of results obtained by the magnetoreflexion and the magneto-piezo-reflection techniques is given in Fig. IV-3 for Ge at room temperature. It is seen that the acoustic modulation of the Landau levels greatly enhances the resonances associated with interband transitions in a magnetic field.

J. G. Mavroides
M. S. Dresselhaus
D. F. Kolesar

* This experiment was carried out using the high field facilities of the National Magnet Laboratory, M.I.T.

Section IV

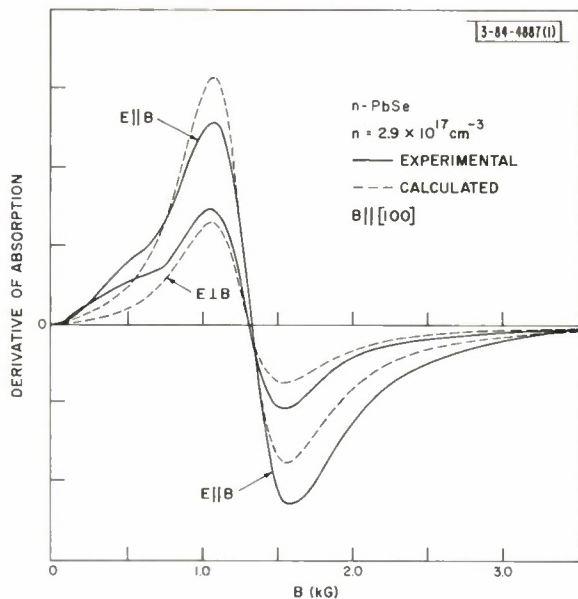


Fig. IV-4. Experimental and theoretical plots of derivative of surface absorption of n-PbSe as function of magnetic field for B along [100] axis. Ordinary ($E \parallel B$) and extraordinary ($E \perp B$) modes are indicated separately.

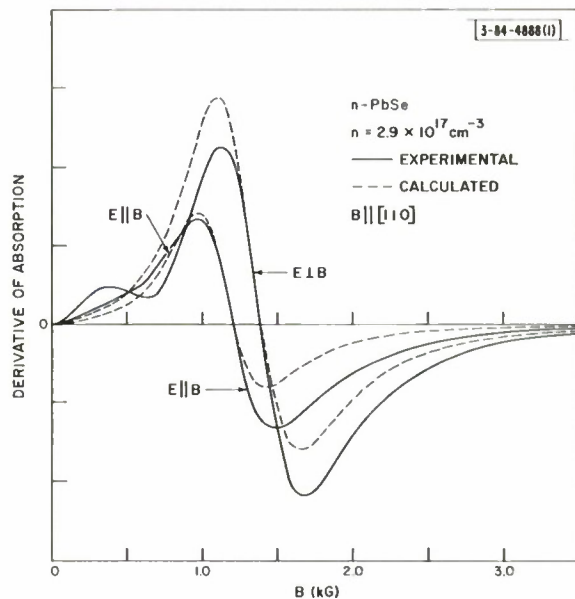


Fig. IV-5. Experimental and theoretical plots of derivative of surface absorption of n-PbSe as function of magnetic field for B along [110] axis. Ordinary ($E \parallel B$) and extraordinary ($E \perp B$) modes are indicated separately.

TABLE IV-1 EFFECTIVE MASS PARAMETERS IN PbSe		
	p-PbSe $p = 1.1 \times 10^{18} \text{ cm}^{-3}$	n-PbSe $n = 2.9 \times 10^{17} \text{ cm}^{-3}$
This Work		
M_f	0.0465 ± 0.002	0.0410 ± 0.002
K	1.8 ± 0.2	1.67 ± 0.2
Cuff, <i>et al.</i> *		
M_f	0.046 ± 0.007	0.044 ± 0.008
K	2.0 ± 0.2	1.75 ± 0.2
*Because of the nonparabolicity of the bands, these values are interpolated from the original data (Ref. 11) to these particular carrier concentrations.		

6. Lineshape Analysis of the Magnetoreflexion Experiment

The following is an abstract of a paper which was presented at the March 1966 meeting of the American Physical Society, Durham, North Carolina:

"Asymmetric lineshapes have been observed in the oscillatory optical reflectivity associated with interband transitions between Landau levels. At constant photon energy, the reflectivity is measured as a function of magnetic field. As the field is increased a typical resonance line in bismuth⁸ consists of a rapid rise in reflectivity followed by a gradual decline. On the other hand, in graphite the lineshape is very different, exhibiting a gradual increase in reflectivity on the low field side and a rapid decrease at high fields. Physical arguments based on the behavior of the real and imaginary parts of the conductivity⁹ suggest that the asymmetry depends sensitively on the relative magnitudes of the plasma frequency ω_p and the pertinent energy band gap ϵ_g . A detailed lineshape calculation is presented with particular emphasis on the two interesting limits $\hbar\omega_p \ll \epsilon_g$ and $\hbar\omega_p \gg \epsilon_g$ which characterize bismuth and graphite, respectively."

M. S. Dresselhaus J. G. Mavroides
G. F. Dresselhaus P. R. Schroeder*

7. Magnetoplasma Cyclotron Resonance in PbSe

Previous measurements¹⁰ of the microwave surface absorption at 70 GHz of PbSe as a function of magnetic field have been extended to n-type material. Experimental curves are shown in Figs. IV-4 and IV-5 for the static magnetic field along the [100] and [110] axes, respectively. As in the case of p-PbSe, good agreement is obtained with curves calculated from the theory of absorption by a high-density plasma under classical skin effect conditions. A $\langle 111 \rangle$ ellipsoid model for the band extrema is assumed. The close fit allows the determination of the conduction band effective mass parameters: m_t , the transverse mass, and $K \equiv m_l/m_t$, the anisotropy ratio. Table IV-1 summarizes these results together with those obtained for p-PbSe, and compares them with the results of Cuff, *et al.*,¹¹ obtained from DC oscillatory magnetoresistance measurements.

Low-field structure, similar to that seen in p-PbSe, is observed and is tentatively attributed to nonlocal effects – perhaps subharmonic Azbel-Kaner resonances.

Efforts are also being made to obtain high-quality samples of different carrier concentrations in order to trace out the variation of the effective mass with carrier concentration to a higher accuracy than has heretofore been possible with other methods.

S. Bermon
W. C. Kernan

8. Luminescence in Magnetic Field of Excitons with Screened Coulomb Potential

The interband recombination radiation from a semiconductor exhibits a shift in its photon energy when a magnetic field is applied. The shift is quadratic at low fields and becomes linear

* Department of Physics, M.I.T.

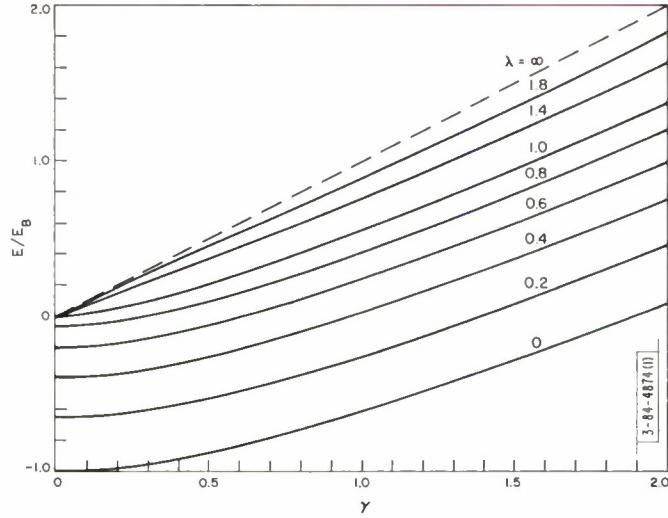


Fig. IV-6. Variation of exciton energy with magnetic field for screened coulomb potential $e^2(\exp[-\lambda r])/r$. Dashed line is for free electrons. $\gamma = 1/2 \hbar\omega_c/E_B$.

at high fields. This behavior can be attributed to the dominance of the coulomb interaction between hole and electron at low field, with a changeover to a linear shift when the diamagnetic energy term dominates the Hamiltonian at high fields. It has been found experimentally that the relative importance of the two terms also depends on the concentration of free charge carriers present, and upon their effective mass. A variational treatment of this problem, which invokes Thomas-Fermi screening to explain the free carrier effects, has been carried out. If the strength of the diamagnetic term relative to the coulomb term is characterized by a parameter $\gamma = \frac{1}{2} \hbar\omega_c/E_B$, it is found that the photon energy shift with magnetic field becomes nearly linear for $\gamma \geq 2.0$ in the absence of screening. As the screening increases, the onset of the linear region occurs at progressively lower values of γ (Fig. IV-6). The variational wave functions used here for $\gamma \leq 2$ give lower energies in the low-field region than those developed for $\gamma \gg 1$ by Yafet, Adams, and Keyes.¹² The results of these calculations have been submitted for publication in the Proceedings of the International Conference on Luminescence, Budapest, 1966.

G. B. Wright

9. Fourier Expansion for Energy Bands of Diamond Lattice

An application of the Fourier expansion technique has been made to study the energy bands for solids which crystallize in the diamond lattice. This class of solids is of particular interest with regard to the Fourier expansion technique because of the large variety of available experimental information on energy band gaps and curvatures for the two semiconductors Si and Ge which have the diamond symmetry.

Since there are two atoms/unit cell, these semiconductors are described in terms of eight interacting s and p energy bands. It would thus seem that the number of Fourier expansion

parameters required to describe the energy bands would be very large. However, the additional spatial symmetry of the diamond lattice greatly restricts the number of independent Fourier coefficients. Furthermore, by requiring time reversal symmetry, the effective mass Hamiltonian can always be written in a form in which these coefficients are real.

Because of the rapid convergence of the Fourier series, a good fit to the experimental data can be obtained using energy bands which include terms only up to next-nearest-neighbor interactions. An explicit application of the method has been made to Si. The band parameters were evaluated using the effective mass determinations from cyclotron resonance measurements¹³ and band gaps determined from analysis of optical data.⁷ It is found that the band parameters are essentially uniquely determined by these experimental data. The results for the energy bands are shown in Fig. IV-7, and a summary of the band gaps and curvatures at high symmetry points in the Brillouin zone is given in Table IV-2. It is of interest that this band model is consistent with observed optical structure not used in the band parameter determination and also provides an explanation for the complicated doping phenomena observed by the electroreflectance technique.¹⁴

G. F. Dresselhaus
M. S. Dresselhaus

B. MAGNETISM

1. Classical Ground Spin States in Normal Cubic Spinels with Nonmagnetic A-Sites

Knowledge of the theoretical magnetic ground state can provide information concerning the relative strengths of the Heisenberg exchange interactions in materials such as CdCr_2Se_4 and ZnCr_2Se_4 . These are normal, cubic spinels with nonmagnetic ions on the A-sites. In our initial report,¹⁵ we defined exchange parameters $U, V, W,$ and X as ratios of the strengths of different next-nearest-neighbor interactions to that of the ferromagnetic nearest-neighbor interaction \bar{J} such that positive values correspond to ferromagnetic coupling. (The class of next-nearest-neighbor interactions is taken to include all superexchange linkages of the form B-anion-anion-B regardless of the physical separation of the magnetic B-sites involved in it.) We displayed the matrix function of these parameters, $\underline{L}'(\vec{k})$, for $\vec{k} = (2\pi/a_0)(0, 0, h)$ and obtained its eigenvalues $\lambda'_\alpha(\sigma)$ and eigenvectors $\Psi'_\alpha(\sigma)$, with $\sigma = \pi h/2$ and $\alpha = 1$ to 4.

According to the classical theory of ground-state spin configurations, a physical spin configuration is proven to be the ground state when its Fourier components can be obtained from the eigenvector associated with the maximum (over all α and \vec{k}) eigenvalue λ_{\max} of $\underline{L}'(\vec{k})$.^{16,17} The ferromagnetic alignment results from $\Psi'_1(0)$, and will be the ground state whenever its eigenvalue $\lambda'_1(0)$ is λ_{\max} . This condition is satisfied throughout the region labeled "ferromagnetic" in Fig. IV-8. Here, the boundaries were computed for $U = V$ and $W = 0$ by comparing certain particular eigenvalues, but the ferromagnetic boundary has been verified by a numerical investigation over all \vec{k} . It moves downward as W increases, and is relatively insensitive to differentiation between U and V .

A collinear antiferromagnetic configuration derived from $\Psi'_4(0)$ is the ground state for sufficiently negative values of X when $(U + V)$ is sufficiently positive. As W increases, this configuration becomes less stable and its boundaries move away from the origin. Its stability region is labeled "antiferromagnetic" in Fig. IV-8.

Section IV

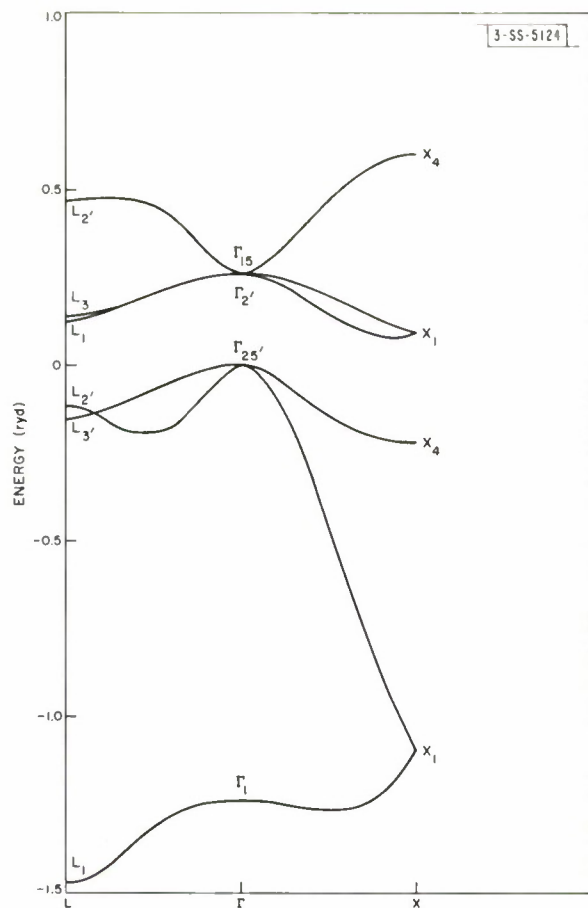


Fig. IV-7. Energy bands in Si calculated by Fourier expansion technique.

TABLE IV-2 SILICON ENERGY GAPS AND CURVATURES					
	Bands	Experiment		Bands	Experiment
	Energy gaps	$\Gamma_{25'} - \Gamma_{15}$		0.259 ryd	Curvatures
$\Gamma_{25'} - \Gamma_{2'}$		0.254 ryd		$M = -3.53$	
$\Gamma_{25'} - \Delta_1$		0.080 ryd		$N = -9.36$	
$L_{2'} - L_1$		0.248 ryd		$m_l = 0.97$	
				Δ_1	$m_t = 0.19$

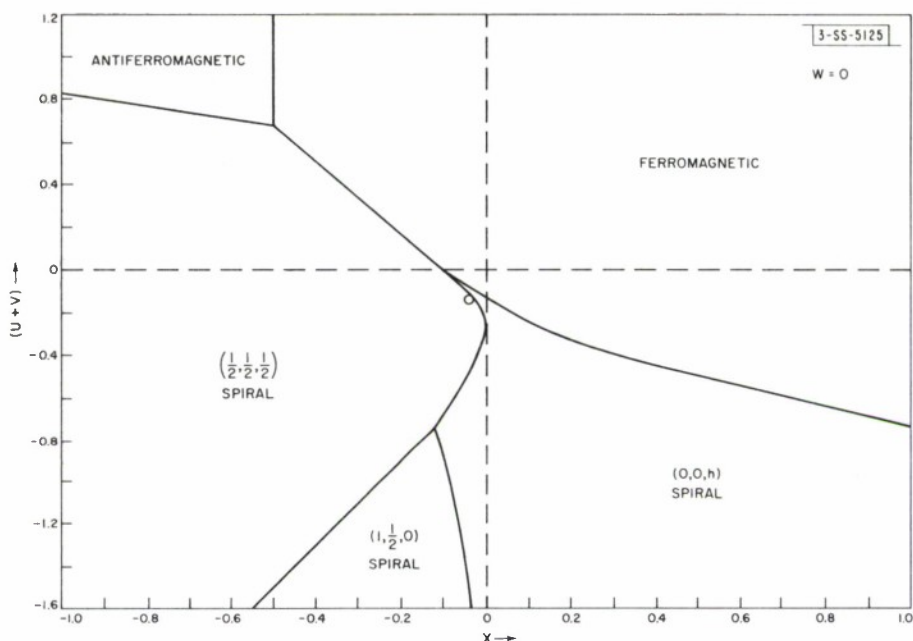


Fig. IV-8. Stable spin configurations in section of next-nearest-neighbor exchange-parameter space.

Our investigation over all \vec{k} established the $(0, 0, h)$ spiral derived from $\Psi_1'(\sigma)$ to be the ground state for sufficiently positive X and sufficiently negative $(U + V)$. When $W = 0$ and $U = V$, it is the ground state for all positive X , but is unstable for negative X except in the immediate neighborhood of its boundary with the ferromagnetic state. Thus, the tentative boundaries between the $(0, 0, h)$ spiral and the $(\frac{1}{2}, \frac{1}{2}, \frac{1}{2})$ and $(1, \frac{1}{2}, 0)$ configurations shown in Fig. IV-8 are overlaid by a region wherein the direction of \vec{k} changes continuously. The stable region of the $(0, 0, h)$ spiral does extend slightly into the negative X quadrant as W increases, but not as much as might be inferred from the corresponding changes in the ferromagnetic boundary. Its boundary is also sensitive to differentiation between U and V , a more negative U tending to stabilize the $(0, 0, h)$ spiral.

The spiral turn angle σ can be determined by neutron diffraction, and its energy can be deduced from susceptibility measurements. These two pieces of information define a unique point in the $X, (U + V)$ plane for each value of W , independent of $(U - V)$ differentiation. Such data are available for ZnCr_2Se_4 .¹⁸ The resulting point for $W = 0$ is shown in Fig. IV-8, where it is seen to lie outside the ground-state region of the $(0, 0, h)$ spiral. An analysis is being made of the range of W and $(U - V)$ for which this point falls in the stable region.

K. Dwight
N. Menyuk

2. Paramagnetic Resonance Linewidth in Chromium Spinels

We have compared the magnetic resonance linewidth, measured in the paramagnetic region, of the insulating chromium spinels CdCr_2S_4 and CdCr_2Se_4 with a theoretical expression based only on dipolar spin-spin interactions (Ref. 19). Neglecting quadrupolar interactions, the linewidth is given by

$$\hbar\Delta\omega = \frac{z\pi^{1/2}S(S+1)D^2}{J[(3/5)\delta + (4/3)S(S+1)(2z-3) + 8S(S+1)\Delta]^{1/2}} \quad (1)$$

where $z = 6$ is the number of nearest magnetic neighbors, $\delta = (2S+3)/(2S-1)$, $\Delta = 1$ for f.c.c. structures, and $S = 3/2$ is the spin quantum number. The dipolar coupling constant is $D = g^2\mu_B^2/r^3$; J is the exchange energy, here determined from the asymptotic Curie temperature (Ref. 20).

- (a) CdCr_2S_4 :— Using $g = 2.00$, $r = 3.62 \text{ \AA}$; and $J/k = 10.4^\circ\text{K}$, the theoretical linewidth is $\Delta H = 113 \text{ Oe}$, while our experimental result, measured on a polycrystalline sample, is $\Delta H = 85 \text{ Oe}$.
- (b) CdCr_2Se_4 :— Using $g = 2.00$, $r = 3.78 \text{ \AA}$, and $J/k = 14^\circ\text{K}$, the theoretical linewidth is $\Delta H = 65 \text{ Oe}$, while our experimental result is $\Delta H = 50 \text{ Oe}$.

The relatively good agreement between theory and experiment shows that neglect of quadrupolar interactions is justified and that, furthermore, the spin-spin interaction does not contain any pseudo-dipolar character. This is the behavior usually observed in ferromagnetic insulators, e.g., in EuS single crystals.²¹ The theoretical expression is given in terms of a single, nearest-neighbor exchange parameter \bar{J} . Actually, it is known²⁰ that there exists a small antiferromagnetic next-nearest-neighbor interaction in the ferromagnetic chalcogenides. Failure to include this explicitly because of complexity of the resulting model gives rise to too small an effective J , leading to a theoretical ΔH on the high side.

R. Weber
P. E. Tannenwald
J. W. Burke

3. High-Temperature Expansions for Spin Correlation Function in Classical Heisenberg Model

The extension of the high-temperature expansions in $1/T$ of the susceptibility χ and the specific heat C for the Heisenberg model with arbitrary spin seems to be highly impractical because of the enormous labor involved.* Nevertheless, there exists a considerable need for more terms in order to study several unresolved problems.

However, many properties of the Heisenberg model are extremely insensitive to the value of S . Thus, useful results may be obtained by calculating the high-temperature expansions of χ and C for the classical Heisenberg model.†

*G. S. Rushbrooke and P. J. Wood, *Mol. Phys.* **1**, 257 (1958), hereafter referred to as R-W.

†The classical Heisenberg magnet has been defined by H. A. Brown and J. M. Luttinger [*Phys. Rev.* **100**, 685 (1955)] as the one for which the spin operators in the Heisenberg model are replaced by classical vectors of length $\sqrt{S(S+1)}$. They observed that the coefficients in the high-T expansion for this classical model can be obtained asymptotically as $S \rightarrow \infty$ in the quantum-mechanical model.

We have found that there are extraordinary simplifications which occur in actually performing the classical calculation. We proceed to discuss these as follows.

All pertinent information can be obtained* from the zero-field spin correlation function

$$\frac{\text{trace } \vec{S}_f \cdot \vec{S}_g e^{-\beta \mathcal{H}}}{\text{trace } e^{-\beta \mathcal{H}}} = \sum_{\ell=0}^{\infty} \frac{(-1)^\ell}{\ell!} \alpha_\ell \beta^\ell \quad (2)$$

between spins \vec{S}_f and \vec{S}_g localized on the sites f and g ; $\beta = 1/kT$, and \mathcal{H} is the spin Hamiltonian for zero magnetic field. For $\ell \geq 1$, the α_ℓ satisfy†

$$\alpha_\ell = \nu_\ell - \sum_{k=0}^{\ell-1} \binom{\ell}{k} \alpha_k \mu_{\ell-k} \quad (3)$$

where $\nu_m = \langle \vec{S}_f \cdot \vec{S}_g \mathcal{H}^m \rangle$, $\mu_m = \langle \mathcal{H}^m \rangle$, and $\langle 0 \rangle = \text{trace } 0 / \text{trace } 1$ denotes the $\beta = 0$ thermal average of the operator O .

The R-W diagrammatic representation‡ of μ_ℓ arises naturally from the fact that $\mathcal{H} = \sum_{ij} J_{ij} \vec{S}_i \cdot \vec{S}_j \equiv \sum_{ij} O_{ij}$; hence, \mathcal{H}^ℓ is a sum of products ΠO_{ij} , and each product contains ℓ factors O_{ij} . For each of the ℓ factors O_{ij} in the product, one draws a straight line connecting sites i and j ; the collection of these ℓ lines corresponding to the entire product is the diagram associated with that product. Thus, one can write $\mu_\ell = \sum_d \mu_\ell(d) = \sum_d P(d) \langle d \rangle$, where $P(d)$ is the number of permutations of the ℓ lines in a diagram d , and $\langle d \rangle = P(d)^{-1} \sum \langle \mathcal{P}(\dots, O_{ij}, \dots) \rangle$, the sum going over all permutations \mathcal{P} of the factors O_{ij} . Similarly, a diagram \bar{d} corresponding to one of the products in $\nu_\ell = \langle \vec{S}_f \cdot \vec{S}_g \mathcal{H}^\ell \rangle$ can be indicated by ℓ straight lines (arising from \mathcal{H}^ℓ) and a wavy line connecting f and g . Writing $\nu_\ell = \sum_{\bar{d}} \nu_\ell(\bar{d})$, where all \bar{d} in the sum include the fixed points f and g , we have $\alpha_\ell = \sum_{\bar{d}} \alpha_\ell(\bar{d})$, with

$$\alpha_\ell(\bar{d}) = \nu_\ell(\bar{d}) - \sum_{k=0}^{\ell-1} \binom{\ell}{k} \sum_{\bar{d}_a, d_b} \alpha_k(\bar{d}_a) \mu_{\ell-k}(d_b) \quad (4)$$



as may be proved from Eq. (3) by induction. The restricted summation \sum^1 is over all partitions of \bar{d} into diagrams \bar{d}_a, d_b such that the sum $\bar{d}_a + d_b = \bar{d}$. Equations (3) and (4) are of general validity and, to the best of our knowledge, are new. Henceforth, we specialize to the classical Heisenberg model.

* The zero-field thermodynamic functions (e.g., free energy, entropy, C , and χ) follow directly from the correlation function. One advantage (over the R-W method) of the formulation in terms of the correlation function is that both C and χ can be obtained from the same diagrammatic calculation. Furthermore, there is additional physical information contained in the correlation function.

† This is simply proved by multiplying both sides of Eq. (2) by $\text{trace } e^{-\beta \mathcal{H}}$ and by expanding everything in powers of β . The "recursion relation" Eq. (3) was first pointed out by K. Dwight (private communication).

‡ G. S. Rushbrooke and P. J. Wood, *Mol. Phys.* **1**, 257 (1958).

There are three simplifying aspects to the classical calculation.

- (a) The requisite traces* (or averages) become integrals and may be evaluated in a tractable closed form.
- (b) The number of diagrams is reduced by roughly an order of magnitude,† for one can ignore all noncontinuous paths‡ and trees. By standard definition, a tree $\bar{d} = \bar{d}_1 + d_2$ may be partitioned into two diagrams \bar{d}_1 and d_2 connected to each other only at one vertex, an "articulation point." For example,  is a tree;  is not. Now, by induction we have proved from Eq. (4) that $\alpha_\ell(\bar{d}) = 0$ for trees and disconnected diagrams. The essential point is that $\langle \bar{d} \rangle = \langle \bar{d}_1 \rangle \langle d_2 \rangle$ §; this follows specifically both from the commutativity and from the isotropy of the classical Heisenberg model.
- (c) All the different products ΠO_{ij} corresponding to the same diagram are equal, so that the summation over all permutations of the O_{ij} may be replaced by a simple multiplicative factor $P(d)$. To illustrate the import of the simplification, we note that ten-line diagrams (which are necessary to extend the calculation by three terms) give rise to as many as 350,000 separate averages – each of which would have to be evaluated individually for the quantum-mechanical calculation!

Thus, the actual effort to extend the high-temperature expansion for general spin is enormously simplified in going to the classical model. Indeed, the classical calculation for the simple models through order six required only a few days, as compared to the several years which were necessary for the corresponding quantum-mechanical calculation. Nonetheless, the labor in adding just one more term to the classical series is still considerably greater than the work in calculating all the previous terms. We have begun extending the calculation of both χ and C for the simple lattices.

H. E. Stanley
T. A. Kaplan

C. TRANSPORT THEORY

1. Space-Time Symmetry of Transport Coefficients

It is often useful to expand a field-dependent transport coefficient in powers of the components of the field, particularly when small values of the field are involved. It is then important to know the space-time symmetry restrictions on the coefficients in the expansion. We indicate here how these restrictions can be obtained in a simple way from basic equations²² derived recently determining space-time symmetry restrictions on field-dependent transport coefficients. Results are presented for the case of thermo-galvanomagnetic coefficients.

* G. S. Rushbrooke and P. J. Wood, *Mol. Phys.* **1**, 257 (1958).

† For example, there are only 1, 1, 2, 2, 5, 7, 18, 32 classical diagrams of ℓ straight lines ($\ell = 2, 3, \dots, 9$, respectively) as against 1, 2, 4, 8, 23, 53, >150, >450 corresponding quantum-mechanical diagrams. [Furthermore, R-W required correspondingly 1, 2, 5, 10, 31, 71, >200, >600 diagrams, because disconnected diagrams contribute to their moment expansion, and not to our Eq. (4); see footnote (§) below.]

‡ A continuous path is one which can be entirely traced out (using every straight line exactly once) from vertex f to vertex g without lifting one's pencil from the paper. This implies that a noncontinuous path has at least one "odd vertex" – i.e., a vertex at which an odd number of lines meet. The odd vertex will contribute an odd number of spin vectors to the integrand of $\nu \rho(\bar{d})$, so that $\nu \rho(\bar{d}) = 0$. Similarly, $\mu \rho(\bar{d}) = 0$ for \bar{d} noncontinuous, so that from Eq. (4) it is easy to see that $\alpha \rho(\bar{d}) = 0$.

§ Since even quantum-mechanically the factorization $\langle \bar{d} \rangle = \langle \bar{d}_1 \rangle \langle d_2 \rangle$ occurs for \bar{d} disconnected, we have used the same inductive argument to prove for the quantum-mechanical Heisenberg model the "linked cluster" theorem, $\alpha \rho(\bar{d}) = 0$ for disconnected \bar{d} . (A disconnected diagram is one which has parts not connected to each other by any lines.)

The procedure is simply to substitute the expansion for the transport coefficient

$$\tau_{B_{\mu} A_{\nu}}(\underline{H}) = \sum_{k=0}^{\infty} \sum_{\alpha_1 \alpha_2 \dots \alpha_k} \tau_{B_{\mu} A_{\nu} \alpha_1 \alpha_2 \dots \alpha_k} H_{\alpha_1} H_{\alpha_2} \dots H_{\alpha_k} \quad (5)$$

on both sides of Eqs. (2.17) and (2.28) of Ref. 22, and to equate like powers of the components of the field for the operators of a set generating the group $K(0)$. The notation used here is defined in Ref. 22. $K(0)$ is the group of quantum-mechanical operators corresponding to space-time symmetry transformations with the property that an element of $K(0)$ leaves the zero-field Hamiltonian for the system invariant.

For thermo-galvanomagnetic coefficients, Eqs. (2.17) and (2.28) of Ref. 22 reduce to the linear homogeneous equations

$$\begin{aligned} \tau_{B_{\mu} A_{\nu} \alpha_1 \alpha_2 \dots \alpha_k} &= \sum_{\kappa \lambda \beta_1 \beta_2 \dots \beta_k} R_{\mu\kappa} R_{\nu\lambda} R_{\alpha_1 \beta_1} R_{\alpha_2 \beta_2} \dots R_{\alpha_k \beta_k} \\ &\times \tau_{B_{\kappa} A_{\lambda} \beta_1 \beta_2 \dots \beta_k} \end{aligned} \quad (6)$$

and

$$\begin{aligned} \tau_{B_{\mu} A_{\nu} \alpha_1 \alpha_2 \dots \alpha_k} &= (-)^k \sum_{\kappa \lambda \beta_1 \beta_2 \dots \beta_k} R_{\mu\kappa} R_{\nu\lambda} R_{\alpha_1 \beta_1} R_{\alpha_2 \beta_2} \dots R_{\alpha_k \beta_k} \\ &\times \tau_{A_{\lambda} B_{\kappa} \beta_1 \beta_2 \dots \beta_k} \end{aligned} \quad (7a)$$

relating the expansion coefficients. The indices of τ , \underline{H} , and R correspond to rectangular components. The matrix $R = D^{-1} = \tilde{D}$ is a 3×3 real orthogonal matrix with D representing the proper rotation part of a quantum-mechanical operator, Eq. (6) applying if the quantum-mechanical operator does not involve time inversion, and Eq. (7a) applying if it does. For thermo-galvanomagnetic coefficients, the same restrictions result from using the Laue²² group $K(0)^L$ of $K(0)$ as result from using $K(0)$ itself.

The equations (6) determine the spatial symmetry restrictions on the expansion coefficients $\tau_{B_{\mu} A_{\nu} \alpha_1 \alpha_2 \dots \alpha_k}$. Equations of this type are well known, are usually derived using properties of tensor transformations, and solving them leads to relations among the coefficients of a type often tabulated.²³⁻²⁵

The similar equations (7a) are new. They determine the symmetry restrictions on $\tau_{B_{\mu} A_{\nu} \alpha_1 \alpha_2 \dots \alpha_k}$ arising from symmetry operations involving time inversion. For equilibrium properties, the symmetry restrictions involving time inversion are, in general, different from those for transport properties. For an equilibrium property, such as isothermal magnetic susceptibility (aside from symmetry in the two tensor indices), with the same tensor character as the thermo-galvanomagnetic coefficients, the space-time symmetry restrictions are determined by Eq. (6) and

Section IV

$$\begin{aligned} \tau_{B_\mu A_\nu \alpha_1 \alpha_2 \dots \alpha_k} &= (-)^k \sum_{\kappa \lambda \beta_1 \beta_2 \dots \beta_k} R_{\mu\kappa} R_{\nu\lambda} R_{\alpha_1 \beta_1} R_{\alpha_2 \beta_2} \dots R_{\alpha_k \beta_k} \\ &\times \tau_{B_\kappa A_\lambda \beta_1 \beta_2 \dots \beta_k} \end{aligned} \quad (7b)$$

which differs from Eq. (7a) only in that $\tau_{A_\lambda B_\kappa \beta_1 \beta_2 \dots \beta_k}$ on the right-hand side of Eq. (7a) is replaced by $\tau_{B_\kappa A_\lambda \beta_1 \beta_2 \dots \beta_k}$; $\tau_{B_\mu A_\nu}$ here denotes the equilibrium property. Space-time symmetry-restricted matrices based on equations of this type have been tabulated by Le Corre²⁶ and by Birss.^{27,28}

Equations (6), (7a), and (7b) hold also if τ is replaced by ${}^s\tau$ or ${}^a\tau$, where s and a denote the components symmetric and antisymmetric with respect to B_μ and A_ν :

$${}^s\tau_{B_\mu A_\nu}(\underline{H}) \equiv 1/2 [\tau_{B_\mu A_\nu}(\underline{H}) + \tau_{A_\nu B_\mu}(\underline{H})] \quad (8a)$$

$${}^a\tau_{B_\mu A_\nu}(\underline{H}) \equiv 1/2 [\tau_{B_\mu A_\nu}(\underline{H}) - \tau_{A_\nu B_\mu}(\underline{H})] \quad (8b)$$

Moreover, Eqs. (7a) and (7b) reduce to the same equations for ${}^s\tau$, since ${}^s\tau_{B_\mu A_\nu \dots} = {}^s\tau_{A_\nu B_\mu \dots}$.

For $k(0)^L$ in category (b),²² Eq. (7a) provides no restrictions. The symmetry restrictions are determined entirely by spatial symmetry and are the same for equilibrium and transport properties.

For $k(0)^L$ in category (a),²² the spatial symmetry restrictions are augmented by Eq. (7a), which requires that

$$\tau_{B_\mu A_\nu \alpha_1 \alpha_2 \dots \alpha_k} = (-)^k \tau_{A_\nu B_\mu \alpha_1 \alpha_2 \dots \alpha_k} \quad (9)$$

representing restrictions imposed by the ordinary Onsager relations $\tau_{B_\mu A_\nu}(\underline{H}) = \tau_{A_\nu B_\mu}(-\underline{H})$; thus,

$${}^s\tau_{B_\mu A_\nu \alpha_1 \alpha_2 \dots \alpha_k} = 0 \quad \text{for } k \text{ odd} \quad (10a)$$

$${}^a\tau_{B_\mu A_\nu \alpha_1 \alpha_2 \dots \alpha_k} = 0 \quad \text{for } k \text{ even} \quad (10b)$$

For equilibrium properties, on the other hand, Eq. (7b) gives

$$\tau_{B_\mu A_\nu \alpha_1 \alpha_2 \dots \alpha_k} = 0 \quad \text{for } k \text{ odd} \quad (11)$$

For $k(0)^L$ in category (c),²² Eq. (7a) leads to new restrictions. For $k = 0$, these are given in Table VI of Ref. 22 for each of the ten crystallographic Laue groups in this category. For $k = 1$, they are given here in Table IV-3 for the electrical conductivity $\underline{\sigma}(\underline{H})$; the corresponding symmetry-restricted matrices for an equilibrium property with the same tensor character can be read directly from the table of piezomagnetic coefficients given in Ref. 26, Table V, by taking the transpose; these symmetry-restricted matrices are also given here in Table IV-3. The

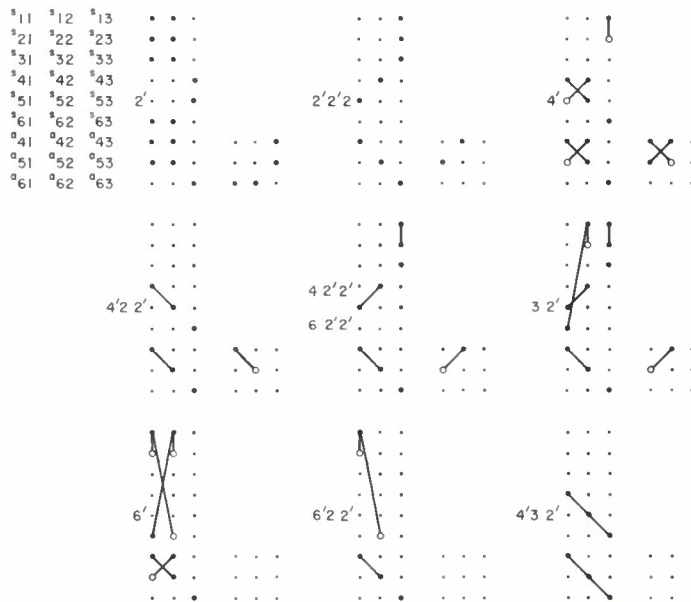
TABLE IV-3
 SYMMETRY-RESTRICTED MATRICES OF CONDUCTIVITY COEFFICIENTS $\sigma_{\mu\nu\alpha}$
 AND CORRESPONDING EQUILIBRIUM PROPERTY COEFFICIENTS

The matrices are given in the form shown at the upper left for each of the ten Laue groups of category (c).²² The first matrix gives $\sigma_{\mu\nu\alpha}$. The second matrix gives the corresponding equilibrium property; only the antisymmetric part is given, since the symmetric part is the same as for $\sigma_{\mu\nu\alpha}$. The choice of axes is as shown in Table V of Ref. 26: the principal axis is along z (or Ox_3). If there exists, in addition, a 2-fold axis ($2, \bar{2} = m, 2', \bar{2}' = m'$) perpendicular to the principal axis, it is taken along Ox_1 ; if more than one, the first in the list $2, m, 2', m'$ is taken along Ox_1 . This choice of axes is also as given on p. 282 of Ref. 24, except that the principal axis is taken along Ox_3 also for monoclinic point groups. The numbers designate the components of $\sigma_{\mu\nu\alpha}$ (or the corresponding equilibrium property). The first of the two indices is an abbreviation for the index pair $\mu\nu$ according to

j	1	2	3	4	5	6	7	8	9
$\mu\nu$	11	22	33	23	31	12	32	13	21

The second index denotes α . The superscripts s and a denote the symmetric and antisymmetric parts according to Eqs. (8). The notation used for the components is that of Ref. 24, p. 123; the key is:

- zero coefficient
- nonzero coefficient
- equal coefficients
- coefficients of equal magnitude but opposite sign



Section IV

transport and equilibrium symmetry-restricted matrices for $k = 1$ are the same for the symmetric part [since Eqs. (7a) and (7b) are equivalent for $^S\tau$], but are seen to be different in every case for the antisymmetric part. In every case, the restrictions on the antisymmetric part of the equilibrium matrix are more stringent in that the equilibrium matrix contains fewer independent components than the transport matrix.

From these results, we can conclude, in particular, that $^a\sigma_{\mu\nu}$ has the same symmetry as the spontaneous magnetization (see Ref. 26, Table IV) and that, apart from a transposition of the coefficient matrix, $^S\sigma_{\mu\nu\alpha} = ^S\hat{\sigma}_{j\alpha}$ has the same symmetry as the matrix for the piezomagnetic effect (see p. 343 of Ref. 27, or p. 144 of Ref. 28). The same two conclusions were drawn recently (albeit for the resistivity rather than the conductivity) by Shtrikman and Thomas²⁹ using a different approach.

The set of equations (6) and (7) for all k contains, in general, more information than the symmetry-restricted \underline{H} -dependent matrices tabulated in Ref. 22. The reason is that the equations determining the symmetry-restricted matrices of Ref. 22 use only the subgroups $K(\underline{H})$ of $K(0)$ rather than $k(0)$ itself; the restrictions corresponding to elements of $k(0)$ not in $K(\underline{H})$ are not taken into account in these symmetry-restricted matrices.

W. H. Kleiner

2. Applications of Frenkel Variational Principle

The behavior of systems too complicated for rigorous analysis is frequently studied with the aid of variational principles which select from among restricted classes of possible wave functions that or those which are "best" approximations. Restricting the class of possible functions controls the difficulty of the analysis; the quality of the approximation is limited by the imagination and patience of the analyst. The Hartree and Hartree-Fock approximations are examples.

A principle due to Frenkel³⁰ permits the study of time-dependent problems and collective excitations of complex systems, topics outside the range of applicability of the Hartree-Fock approximation. This principle leads to the so-called "time-dependent Hartree-Fock approximation," or RPA, for many-Fermion wave functions limited to the class of single determinants. We have studied more-general wave functions of the BCS³¹ type appropriate to the superconducting state, rederiving (with less labor) the "S-wave coupling" results of Bardasis and Schrieffer³² on the spin excitation spectrum of superconductors, and finding (with rather more labor) a somewhat more general form of some excitations discovered by Anderson.³³

We are currently applying the principle to electrical conduction problems in narrow-band systems.

L. L. Van Zandt

D. QUANTUM ELECTRONICS

1. Stimulated Raman Emission in CaWO_4

Stimulated Raman emission has been observed in several single crystals of calcium tungstate – both pure and Nd^{3+} -doped – at room temperature and near 20°K . At room temperature, only the vibrational mode at 911 cm^{-1} is excited. At low temperature, the 911 cm^{-1} plus the 326 cm^{-1} lines are observed in the pure crystal; but, in a 0.3%-doped $\text{Nd}^{3+}:\text{CaWO}_4$, an entirely

different CaWO_4 Raman line at 83 cm^{-1} appears, and furthermore very strongly (7 Stokes and 3 anti-Stokes lines). Enhancement of the Raman cross section through interaction with Nd^{3+} centers is being investigated.

P. E. Tannenwald
H. J. Zeiger
F. H. Perry

2. Temperature Dependence of Incoherent Second Harmonic Light Scattering in Liquids

Measurements of second harmonic incoherent scattering in water have been extended to temperatures above room temperature (Fig. IV-9). The upturn in scattering at the highest temperature is believed to be a spurious effect, arising from nonequilibrium temperature inhomogeneities. It becomes less prominent as the furnace is improved to reduce the difference in temperature readings between thermocouples which bracket the sample. A thermal gradient does not orient the molecules, but rather modulates the density, and therefore the molecular interaction. It should be remembered that only orientation inhomogeneity, not density inhomogeneity, leads to inhomogeneous-induced second-order polarization, and therefore to scattering, in a system of identical molecules. This difference is due to the rotational symmetry of a third rank (polarizability) tensor.

The rapid decrease of scattering to a plateau, with increasing temperature, probably represents dissociation of clusters of similarly oriented molecules into increasingly freely rotating individuals, whose mutual correlation time finally becomes short compared to the pulse duration, 10^{-8} sec. Since the molecules of a rigid cluster scatter coherently, i.e., with constructive interference, clustering of similarly oriented molecules increases the scattering.

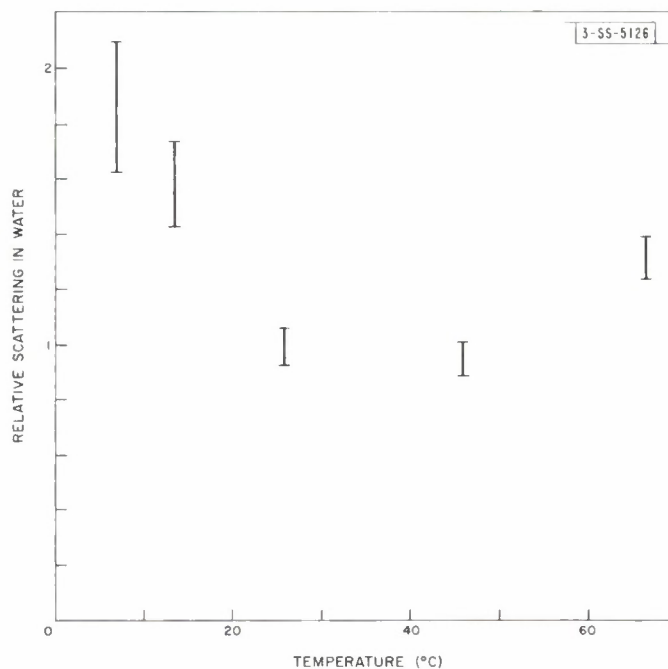


Fig. IV-9. Temperature dependence of incoherent second harmonic scattering in water.

Section IV

It is desirable to deduce the individual molecular polarizability tensor β_{ijk} from independent molecular scattering, and to use it to calculate the polarizabilities of possible clusters. These might then be used to calculate the scattering from various cluster distributions, for comparison with the measured scattering, in order to deduce the cluster distribution as a function of temperature. Since absorption and dispersion are very small in water, Kleinman's theorem shows that the β_{ijk} for the water molecule should have only three independent elements, β_{311} , β_{322} , and β_{333} , and that the scattering in liquid water involves only two characteristic numbers. Figure IV-9 indicates that the scattering in water at room temperature has fallen approximately to the level attributed to independent molecule scattering. Terhune, *et al.*,³⁴ measured the scattering at room temperature in four different states of incident or scattered polarization. The results are consistent with symmetry requirements on the liquid. However, when the scattering quantities are formulated in terms of the β_{ijk} , no solutions are possible for the β_{ijk} without discrepancies much larger than the experimental uncertainties. Hence, the water molecules do not scatter independently. This conclusion is not necessarily inconsistent with independently rotating molecules, since electronic intermolecular perturbations can cause the polarizabilities of different molecules to be different. At sufficiently high liquid temperatures, or at worst in the vapor state, the above method of finding the β_{ijk} should be feasible.

It is now known that self-focusing of high-power laser beams in liquids involves alignment of the molecules with their direction of maximum polarizability along the optical electric field,³⁵ with even complete alignment attainable. The possibility has been considered of coherent mixing in liquids whose inversion symmetry is removed in this way. It is shown here that a noncentrosymmetric liquid must still have molecules which lack improper symmetry operations. Consider a liquid which is aligned in the z-direction. Among its symmetries are any rotation about the z-direction, and 180° rotation about any axis in the x-y plane. The molecules have their maximum polarizabilities along the z-direction, which must thus be one of the principal axes of the molecular polarizability tensor. If the molecule has a reflection plane, such a plane must either be perpendicular to the z-axis or else contain the z-direction. Then a symmetry operation of the liquid is reflection in the plane and rotation by 180° about the direction perpendicular to it, which is inversion. If the molecule has a rotation-reflection axis, the polarizability is the same for all directions perpendicular to the rotation-reflection axis. That axis must be along or perpendicular to the z-direction. Therefore, the liquid has complete rotational symmetry about that axis, and one of the rotations combines with the rotation-reflection to give the inversion.

D. L. Weinberg

3. Maser Amplification of Interstellar OH Emission

The anomalously intense, polarized, and narrow-band microwave emission of interstellar OH hyperfine transitions which has been reported³⁶ can be explained by maser amplification of spontaneous emission. We propose a model for obtaining the necessary inverted population by means of near-ultraviolet pumping of the lower Λ -doublet hyperfine state populations into the upper Λ -doublet states via radiative cascading from the electronic states excited by UV

absorption.* We show that selective absorption of the strongest-absorbed wavelengths of the UV pump by intervening layers of OH will provide a large region of net inversion. By exhibiting the gain and polarization properties of the normal electromagnetic modes of a medium which is optically pumped in the presence of a magnetic field, we are able to predict nearly circularly polarized emission with brightness temperatures equal to or greater than those observed, $> \sim 10^6$ °K. Furthermore, the nonlinear analysis of gain saturation and mode suppression indicates that a single dominant mode will propagate in a given direction with a very high degree of polarization.

M. M. Litvak M. L. Meeks
A. L. McWhorter H. J. Zeiger

REFERENCES

1. A. H. Kahn and A. J. Leyendecker, *Phys. Rev.* 135, A1321 (1964).
2. Solid State Research Report, Lincoln Laboratory, M. I. T. (1965:3), p. 42, DDC 629048, H-705.
3. R. G. Wheeler and J. O. Dimmock, *Phys. Rev.* 125, 1805 (1962).
4. E. J. Johnson and D. M. Larsen, *Phys. Rev. Letters* 16, 655 (1966).
5. W. S. Boyle and A. D. Brailsford, *Phys. Rev.* 107, 903 (1957).
6. W. E. Engeler, *et al.*, *Phys. Rev. Letters* 14, 1069 (1965).
7. G. W. Gobeli and E. O. Kane, *Phys. Rev. Letters* 15, 142 (1965).
8. R. N. Brown, J. G. Mavroides, and B. Lax, *Phys. Rev.* 129, 2055 (1963).
9. M. S. Dresselhaus and G. F. Dresselhaus, *Phys. Rev.* 125, 499 (1962).
10. Solid State Research Report, Lincoln Laboratory, M. I. T. (1966:1), p. 41, DDC 632998, H-721.
11. K. F. Cuff, *et al.*, Proceedings of the 7th International Conference on the Physics of Semiconductors, Paris, 1964 (Dunod, Paris, 1964), p. 677.
12. Y. Yafet, E. N. Adams, and R. W. Keyes, *J. Phys. Chem. Solids* 1, 137 (1956).
13. J. C. Hensel and G. Fcher, *Phys. Rev.* 129, 1041 (1963).
14. B. O. Seraphin and N. Bottka, *Phys. Rev. Letters* 15, 104 (1965); B. O. Seraphin, *Bull. Am. Phys. Soc.* 11, 272 (1966).
15. Solid State Research Report, Lincoln Laboratory, M. I. T. (1966:1), p. 50, DDC 632998, H-721.
16. D. H. Lyons and T. A. Kaplan, *Phys. Rev.* 120, 1580 (1960).
17. D. H. Lyons, *et al.*, *Phys. Rev.* 126, 540 (1962).
18. R. Plumier, *J. Appl. Phys.* 37, 964 (1966).
19. B. R. Cooper and F. Keffer, *Phys. Rev.* 125, 896 (1962).
20. Solid State Research Report, Lincoln Laboratory, M. I. T. (1965:2), p. 60, DDC 624611, H-686; and (1965:3), p. 45, DDC 629048, H-705.

* UV pumping has been independently proposed by F. Perkins, T. Gold, and E. E. Salpeter (to be published in the Astrophysical Journal) in order to invert selected magnetic hyperfine sublevels, with no net inversion of the upper state.

Section IV

21. S. vonMolnar and A. W. Lawson, *Phys. Rev.* 139, A1598 (1965).
22. W. H. Kleiner, *Phys. Rev.* 142, 318 (1966), DDC 635328.
23. H. Jagodzinski, *Encyclopedia of Physics*, edited by S. Flugge (Springer-Verlag, Berlin, 1955), Vol. 7/1, p. 1.
24. J. F. Nye, *Physical Properties of Crystals* (Oxford University Press, London, 1960).
25. C. S. Smith, *Solid State Physics*, edited by F. Seitz and G. Turnbull (Academic Press, New York, 1958), Vol. 6, p. 175.
26. Y. Le Corre, *J. Phys. Radium* 19, 750 (1958).
27. R. R. Birss, *Rept. Progr. Phys.* 26, 307 (1963).
28. ———, *Symmetry and Magnetism* (Wiley, New York, 1964).
29. S. Shtrikman and H. Thomas, *Solid State Commun.* 3, 147 (1965), and erratum in *Solid State Commun.* 3, No. 9 (1965).
30. J. Frenkel, *Wave Mechanics, Advanced General Theory* (Clarendon Press, Oxford, 1934).
31. J. Bardeen, L. Cooper, and R. Schrieffer, *Phys. Rev.* 108, 1175 (1957).
32. A. Bardasis and R. Schrieffer, *Phys. Rev.* 121, 1050 (1961).
33. P. W. Anderson, *Phys. Rev.* 112, 1900 (1958).
34. R. W. Terhune, P. D. Maker, and C. M. Savage, *Phys. Rev. Letters* 14, 681 (1965).
35. P. Lallemand and N. Bloembergen, *Phys. Rev. Letters* 15, 1010 (1965).
36. S. Weinreb, *et al.*, *Nature* 200, 829 (1963); B. J. Robinson, *et al.*, *Nature* 202, 989 (1964); R. X. McGee, *et al.*, *Nature* 208, 1195 (1965); S. Weinreb, *et al.*, *Nature* 208, 440 (1965), DDC 626888; N. H. Dieter, H. Weaver, and D. W. R. Williams, *Sky and Telescope* XXXI, No. 3, 132 (1966); A. H. Barrett and A. E. E. Rogers, *Nature* (in press); M. L. Meeks, J. A. Ball, and J. C. Carter, Abstract Paper presented at American Astronomical Society, Hampton, Virginia, 28-31 March 1966.

DOCUMENT CONTROL DATA - R&D

(Security classification of title, body of abstract and indexing annotation must be entered when the overall report is classified)

1. ORIGINATING ACTIVITY <i>(Corporate author)</i> Lincoln Laboratory, M.I.T.		2a. REPORT SECURITY CLASSIFICATION Unclassified	
		2b. GROUP None	
3. REPORT TITLE Solid State Research			
4. DESCRIPTIVE NOTES <i>(Type of report and inclusive dates)</i> Quarterly Technical Summary - 1 February through 30 April 1966			
5. AUTHOR(S) <i>(Last name, first name, initial)</i> McWhorter, Alan L.			
6. REPORT DATE 15 May 1966		7a. TOTAL NO. OF PAGES 76	7b. NO. OF REFS 112
8a. CONTRACT OR GRANT NO. AF 19 (628)-5167		9a. ORIGINATOR'S REPORT NUMBER(S) Solid State Research (1966:2)	
b. PROJECT NO. 649L		9b. OTHER REPORT NO(S) <i>(Any other numbers that may be assigned this report)</i> ESD-TR-66-207	
c.			
d.			
10. AVAILABILITY/LIMITATION NOTICES Distribution of this document is unlimited.			
11. SUPPLEMENTARY NOTES None		12. SPONSORING MILITARY ACTIVITY Air Force Systems Command, USAF	
13. ABSTRACT This report covers in detail the solid state research work at Lincoln Laboratory for the period 1 February through 30 April 1966. The topics covered are Solid State Device Research, Optical Techniques and Devices, Materials Research, and Physics of Solids.			
14. KEY WORDS			
solid state devices	optical pumping	electronic band	magnetoplasma
solid state physics	electron beam	structure	magnetism
optical techniques	excitation	polaron resonance	transport theory
and devices	vapor growth	coulomb potential	quantum electronics
materials research	high-power lasers	Fourier expansion	photoluminescence
laser research	chemical analysis	magnetoreflexion	